Atomic structure and hierarchical assembly of a cross-β amyloid fibril

Anthony W. P. Fitzpatrick[a,b], Galia T. Debelouchina[c], Marvin J. Bayro[c], Daniel K. Clare[d], Marc A. Caporini[c], Vikram S. Bajaj[c], Christopher P. Jaroniec[c], Luchun Wang[d], Vladimir Ladizhansky[c], Shirley A. Müller[e], Cait E. MacPhee[f], Christopher A. Waudby[a,d], Helen R. Mott[g], Alfonso De Simone[a,h], Tuomas P. J. Knowles[a], Helen R. Saibil[d], Michele Vendruscolo[a], Elena V. Orlova[d], Robert G. Griffin[c], and Christopher M. Dobson[a,1]

[a]Department of Chemistry, University of Cambridge, Cambridge CB2 1EW, United Kingdom; [b]Cavendish Laboratory, University of Cambridge, Cambridge CB3 0HE, United Kingdom; [c]Francis Bitter Magnet Laboratory and Department of Chemistry, Massachusetts Institute of Technology, Cambridge, MA 02139; [d]Institute of Structural and Molecular Biology, Birkbeck College, London WC1E 7HX, United Kingdom; [e]Maurice E. Müller Institute, Biozentrum, CH-4056 Basel, Switzerland; [f]School of Physics, University of Edinburgh, Edinburgh EH9 3JZ, United Kingdom; [g]Department of Biochemistry, University of Cambridge, Cambridge CB2 1GA, United Kingdom; and [h]Division of Molecular Biosciences, Imperial College London, London SW7 2AZ, United Kingdom

The cross-β amyloid form of peptides and proteins represents an archetypal and widely accessible structure consisting of ordered arrays of β-sheet filaments. These complex aggregates have remarkable chemical and physical properties, and the conversion of normally soluble functional forms of proteins into amyloid structures is linked to many debilitating human diseases, including several common forms of age-related dementia. Despite their importance, however, cross-β amyloid fibrils have proved to be recalcitrant to detailed structural analysis. By combining structural constraints from a series of experimental techniques spanning five orders of magnitude in length scale—including magic angle spinning nuclear magnetic resonance spectroscopy, X-ray fiber diffraction, cryoelectron microscopy, scanning transmission electron microscopy, and atomic force microscopy—we report the atomic-resolution (0.5 Å) structures of three amyloid polymorphs formed by an 11-residue peptide. These structures reveal the details of the packing interactions by which the constituent β-strands are assembled hierarchically into protofilaments, filaments, and mature fibrils.

It is well established that a wide variety of peptides or proteins without any evident sequence similarity can self-assemble into amyloid fibrils (1, 2). These structures have many common characteristics, typically being 100–200 Å in diameter and containing a universal "cross-β" core structure composed of arrays of β-sheets running parallel to the long axis of the fibrils (3). These fibrillar states are highly ordered, with persistence lengths of the order of microns (4) and mechanical properties comparable to those of steel and dragline silk, and much greater than those typical of biological filaments such as actin and microtubules (5). Amyloid fibrils can also possess very high kinetic and thermodynamic stabilities, often exceeding those of the functional folded states of proteins (6), as well as a greater resistance to degradation by chemical or biological means (7). Several functional forms of proteins that exploit these properties have been observed in biological systems (8). More generally, however, the conversion of normally soluble functional proteins into the amyloid state is associated with many debilitating human disorders, ranging from Alzheimer's disease to type II diabetes (1, 9). Our understanding of the nature of this type of filamentous aggregate has greatly improved in recent years (3, 10–19), particularly through the structural determination of their elementary β-strand building blocks (20) and the characterization of their assembly into cross-β steric zippers (21, 22). However, a thorough understanding of the hierarchical assembly of these individual structural elements into fully-formed fibrils, which display polymorphism but possess a range of generic features (23), has so far been limited by the absence of a complete atomic-resolution cross-β amyloid structures (2).

We report here the simultaneous determination of the atomic-resolution structures of a cross-β amyloid fibril and two polymorphic variants, formed by an 11-residue fragment of the protein transthyretin, TTR(105–115) (20). These fibrils have the classic amyloid morphology, being 100–200 Å in diameter and typically 1–3 μm in length (*SI Appendix*, Fig. S1). We have achieved this objective by bringing together a set of complementary biophysical techniques to provide atomic structures of these complex aggregates. Specifically, we have combined interatomic structural restraints from magic angle spinning (MAS) nuclear magnetic resonance (NMR) spectroscopy with high-resolution electron density maps from cryoelectron microscopy (cryo-EM), together with data from X-ray fiber diffraction, scanning transmission electron microscopy (STEM), and atomic force microscopy (AFM) measurements. Our results reveal the molecular basis of the stability and polymorphism of these amyloid fibrils by defining at high resolution the variety of structural elements in their hierarchical self-assembly.

Results

Assembly of Individual Molecules into β-Sheet Arrays. A large number of intramolecular distance and torsion angle restraints (76 total) have been measured previously using MAS NMR methods, resulting in the high-resolution structure of the individual TTR(105–115) molecules in amyloid fibrils (20). To extend these studies to probe higher-order elements in the amyloid assemblies by identifying site-specific intermolecular restraints, we prepared eight different samples, each having a single isotopically labeled carbonyl atom per TTR(105–115) molecule at one of the residues I107 to P113 and S115. Double quantum dipolar recoupling experiments (24) on these singly labeled samples provided eight high-precision (<0.2 Å), intrasheet $^{13}CO–^{13}CO$ distance restraints (*SI Appendix*, Table S1 and Fig. S2A). The restraints span the entire backbone of the extended β-strand conformation adopted by TTR(105–115) peptides in fibrils (*SI Appendix*, Table S1 and Fig. S2A) and unequivocally define a parallel, in-register arrangement of neighboring strands within the β-sheets.

Although knowledge of the intrasheet registry drastically reduces the number of permutations for the peptide molecules within the structure of the protofilaments, the number of possible intersheet arrangements is still very large (22). To address the challenge of defining this level of structural detail, we prepared two separate TTR(105–115) samples labeled uniformly with ^{13}C and ^{15}N isotopes at (underscored) residues YTIA**AALL**SPYS and **YTIA**ALL**SPYS** to characterize selectively the intermolecular packing of adjacent β-sheets in the fibrils. Internuclear distance restraints from Z-filtered transferred echo double resonance (ZF-TEDOR) (25) and rotational resonance in the tilted frame width (R2TRW) (26) experiments on centrally labeled YTIA**AALL**SPYS samples (*SI Appendix*, Table S2 and Fig. S2B) strongly suggest that the β-strands in a given β-sheet are antiparallel to those in the adjacent β-sheet.

To obtain further information on this crucial issue, we carried out additional ZF-TEDOR experiments using terminally labeled **YTIA**ALL**SPYS** samples and observed three clearly resolved cross-peaks (Fig. 1A and *SI Appendix*, Fig. S3). The mixing-time dependence of the cross-peak intensities yielded three highly precise (±0.3 Å) internuclear distances (*SI Appendix*, Table S2). This precision establishes an antiparallel intersheet stacking of β-sheets because not only do the contacts arise between residues at opposite ends of the TTR(105–115) molecule, but also the measured distances are much too short to occur either intramolecularly or within a parallel, in-register β-sheet. These measurements were further complemented by proton-driven ^{13}C spin diffusion (PDSD) (27) experiments (Fig. 1B and *SI Appendix*, Fig. S4) on the **YTIA**ALL**SPYS** sample; cross-peaks from these spectra provided a total of 16 ^{13}C–^{13}C intersheet restraints (*SI Appendix*, Table S2 and Fig. S2B). The complete set of 23 intersheet distance restraints (*SI Appendix*, Table S2 and Fig. S2B) reveals the specific manner in which adjacent β-sheets within the fibril are stacked in an antiparallel arrangement, thereby solving the first crucial aspect of the assembly of these multimolecular species.

The quantitative intersheet constraints between L111 and A108 and A109 (Fig. 1C, blue dashed lines), between A108 and S112 and P113 (Fig. 1C, red dashed lines), and between I107 and S112 (Fig. 1C, red dashed lines) are consistent only with a structure in which the even-numbered side chains, TALSY (Fig. 1C, violet sticks), are packed against odd-numbered side chains, YIALPS (Fig. 1C, orange sticks), thus yielding an even–odd–even–odd interface between the sheets (Fig. 1C). This arrangement means that the side chains of all residues in the sequence appear both on the internal (dry) and external (wet) faces of each protofilament, and so in principle two sets of chemical shifts could be expected for each site. Indeed, some side chains do exhibit clear peak doubling, for example, I107Cδ, Cγ1 and Cγ2 and S112Cα and Cβ as illustrated in *SI Appendix*, Fig. S5. Additionally, Y105 displays two conformations for the $^{15}NH_3^+$ and $^{13}C\alpha$ (*SI Appendix*, Fig. S5). Because some side chains are more prone to dispersion than others, the chemical shift differences between the two different conformations for other cross-peaks are not resolved but contribute to the inhomogeneous broadening of the cross-peaks. For example, the linewidths of A108Cβ, A109Cβ, L110Cδ, and L111Cδ are ~1.0–1.2 ppm. Similar doubling of some peaks has also been detected for polyglutamine (poly-Q) fibrils, although in this case this phenomenon is likely to arise from an antiparallel β-sheet structure, which is also a packing geometry leading to residues alternately pointing into (buried) and out (solvent exposed) of the fibril (28, 29). The intensities of the peaks that exhibit doubling in *SI Appendix*, Fig. S5 are not 1:1, unlike the peaks in poly-Q spectra (28, 29), because here, the solvent exposed side chains are more likely to be dynamic than those buried in the dry interface between the β-sheets.

A summary of the restraints used in the calculation of the protofilament structure is given in *SI Appendix*, Table S1 (intrasheet; *SI Appendix*, Fig. S2A) and *SI Appendix*, Table S2 (intersheet; *SI Appendix*, Fig. S2B). The resulting set of structures, which were calculated with an average of 10 restraints per residue, has a backbone heavy atom root mean square deviation to the mean of the 20 lowest energy conformers in the NMR ensemble of 0.4 Å for the backbone and 0.7 Å for all heavy atoms (*SI Appendix*, Fig. S6). There are no residues with torsion angles in disallowed regions of the Ramachandran plot (*SI Appendix*, Table S3). Complete details concerning the structure calculations and statistics are provided in *SI Appendix, SI Materials and Methods* and Table S3.
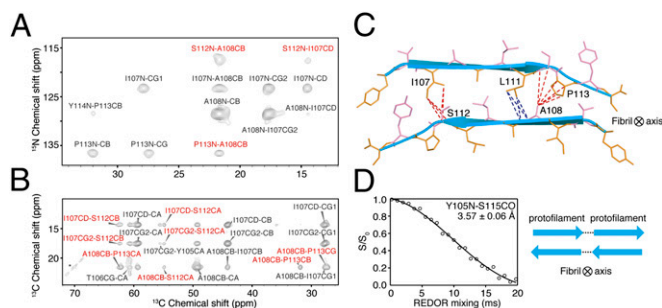
Atomic Structure of the Cross-β Protofilaments. The results presented above define a parallel, in-register β-sheet geometry within the sheets of the TTR(105–115) fibrils (Fig. 2A and Movie S1), indicating a full complement of nine backbone–backbone hydrogen bonds (Fig. 2A) along the entire length of the molecule—i.e., involving all residues but the proline at position 113. The fact that this optimized interbackbone hydrogen-bonding network adopts this particular arrangement indicates that the intrinsically more favorable hydrogen-bonding pattern found in antiparallel β-sheets is offset by the juxtaposition of side chains with identical hydrophobic and hydrophilic character in the ordered self-assembly of these amphiphilic molecules. The in-register alignment of matching residues generates very tight packing (shape complementarity = 0.76; Fig. 2A), also maximizing favorable hydrophobic and van der Waals side-chain contacts along the long axis of the fibril (14); in addition, the structures may gain further stabilization through π–π stacking of the tyrosine aromatic rings (10) at the termini of the TTR(105–115) molecule (Fig. 2 A and B). The low degree of left-handed twist (~1° between successive β-strands; Fig. 2B and *SI Appendix, SI Supporting Equation*) favored by the constituent parallel β-sheets of the fibrils is similar to the nearly flat β-sheets proposed in models of SH3 (11) and insulin (12) fibrils and limits lateral growth in the sheet–sheet direction (Fig. 2 B and C), thus discriminating individual fibrils from 3D amyloid-like microcrystals (21, 22).

Fig. 1. MAS NMR experiments used to probe the intermolecular arrangement of TTR(105–115) fibrils. (A and B) Shown are 2D ^{13}C–^{15}N ZF-TEDOR (τ_{mix} = 10.24 ms) (A) and 2D ^{13}C–^{13}C PDSD (τ_{mix} = 200 ms) (B) MAS NMR spectra of TTR(105–115) U–^{15}N,^{13}C labeled as **YTIA**ALL**SPYS** and recorded at $\omega_{0H}/2\pi$ = 750 MHz and $\omega_r/2\pi$ = 12.5 kHz and $\omega_{0H}/2\pi$ = 900 MHz and $\omega_r/2\pi$ = 11 kHz, respectively, and T = 280 K. The spectra were used to constrain the intermolecular distances between the β-sheets within the TTR(105–115) protofilament. In the two spectra, intermolecular and intramolecular cross-peaks are labeled in red and black, respectively, and all cross-peaks have been assigned. (C) A cross-section of the TTR(105–115) protofilament depicting the sheet-to-sheet interface and the 11 distance constraints labeled in the spectra of A and B (red lines). The blue lines denote four additional distances between L111–$^{13}C\delta1$ and –$^{13}C\delta2$ and A109–^{15}N and A108–^{13}CO detected in additional spectra of a sample labeled as YTIA**AALL**SPYS. The complete set of 23 intersheet distance restraints is shown in *SI Appendix*, Fig. S2B. Odd- and even-numbered side chains are shown as orange and violet sticks, respectively, with secondary structure shown in a cyan ribbon representation. (D) ^{13}C–^{15}N REDOR data obtained from a TTR(105–115) sample labeled as Y105–^{15}N, S115–$^{13}CO_2H$ (**Y**TIAALLSPY**S**) and designed to detect interprotofilament contacts in the fibril. The intermolecular ^{13}C–^{15}N interaction between the terminal ^{15}N and ^{13}C atoms corresponds to a distance of 3.57 ± 0.06 Å, consistent with a head-to-tail protofilament arrangement as illustrated in *Right*. The curve was fitted by using the program SPINEVOLUTION (*SI Appendix, SI Materials and Methods*).
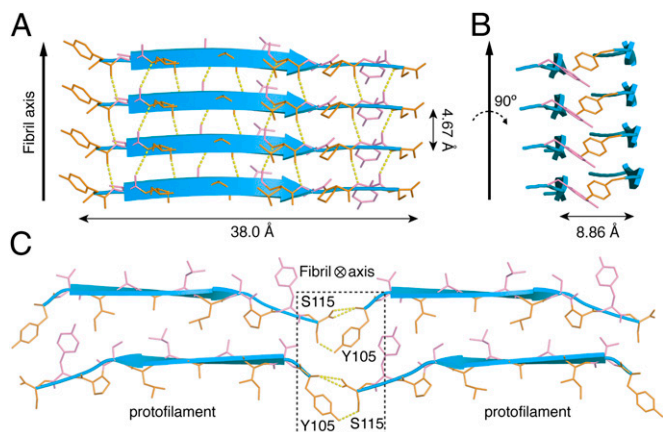
BIOCHEMISTRY

Fig. 2. Atomic-resolution structure of the TTR(105–115) protofilament determined by MAS NMR. The structures (calculated with CNSsolve; see *SI Appendix, SI Materials and Methods*) have a rmsd of ~0.4 Å for the backbone and 0.7 Å for all atoms. Odd- and even-numbered side chains are shown as orange and violet sticks, respectively, with secondary structure shown in a cyan ribbon representation. (*A*) The β-sheet viewed perpendicularly to the fibril axis illustrating the parallel in-register β-strands and the hydrogen bonds defining the β-sheet (yellow lines). The conformation was determined from eight $^{13}C=O–^{13}C=O$ double quantum distance measurements and one $^{13}C=O–^{13}C=O$ REDOR distance measurement (*SI Appendix*, Table S1). (*B*) Cross-sectional view of the two-sheet protofilament along the peptide chain direction. There is a sheet–sheet offset of approximately one-fifth the separation of hydrogen-bonded β-strands (i.e., 0.2×4.67 Å = 0.93 Å) shown clearly by the interdigitation of the Y105 (orange sticks) and Y114 (violet sticks) side chains. (*C*) Protofilament–protofilament interface viewed looking down the long axis of the fibril showing the head-to-tail packing arrangement. Interprotofilament hydrogen bonds between the terminal C=O and N–H groups and between the Y105 OH atoms and the S115 Oγ atoms are depicted as yellow dashes.

The structure shows that in-register, parallel β-sheets stack antiparallel to one another via a C_2 axis parallel to the intersheet direction (Fig. 2*C* and Movie S1) to create a two-sheet protofilament as suggested in previous models of cross-β fibrils (11, 12). There is also an average sheet–sheet shift of 0.9 ± 0.6 Å, which is approximately one-fifth of the separation of hydrogen-bonded β-strands (Fig. 2*B*). This staggered arrangement results in the burial of even-numbered side chains, TALSY (Fig. 2*B*, violet sticks), on one sheet between two sets of odd-numbered side chains, YIALPS (Fig. 2*B*, orange sticks), on the opposite face and vice versa, in a highly specific manner similar to the "parallel, face-to-back, up–down" class of steric zipper (22). The self-complementary interdigitation of the side chains of two β-sheets (shape complementarity = 0.79; Fig. 2 *B* and *C*) creates a tightly packed, hydrophobic core composed primarily of the contiguous hydrophobic stretch IAALL. The ~1-Å sheet–sheet shift, however, leads to incompletely paired β-strands at the fibril ends (13) (Fig. 2*B* and Movie S1) with exposed hydrophobic residues and unsatisfied hydrogen bonds. The staggering of the cross-sheet stack therefore breaks the symmetry of the growing ends of the fibril, resulting in a single binding site for the addition of monomers (30). The offset of the sheets is also likely to make the fibrils more resistant to bending and stretching forces and thus less prone to fracture, which can play key roles in the kinetics of self-templated aggregation (31).

Overall Architecture of the Mature Fibrils. Because fibrils are typically composed of between two and six protofilaments (12), a vast number of interprotofilament packing arrangements are possible, for example, as observed in Aβ fibrils (16, 17, 19, 32). Although variations in intrasheet and intersheet stacking within protofilaments give rise to molecular-level polymorphism (15), interprotofilament arrangements represent an ultrastructural polymorphism (33) that can

result in vast numbers of fibrils with distinct morphologies, where the nature of the interactions are unlikely to affect significantly the chemical shifts of any of the residues (12). Knowledge of the atomic structure of the protofilaments from the MAS NMR analysis, however, provides clues as to the possible higher-order packing interfaces. We therefore have combined single-particle and helical cryo-EM approaches (11, 16) to determine the overall structure of the complete fibrils formed by TTR(105–115). The fibrils are observed to be twisted ribbons with regular cross-over distances ranging from 850 to 1,000 Å (Fig. 3 *A*–*C*, and *SI Appendix*, Fig. S1 and Table S4). Three prominent fibril types were identified (Fig. 3 *A*–*C*) with distinct widths between crossovers (84 Å, Fig. 3 *A* and *D*; 121 Å, Fig. 3 *B* and *E*; and 154 Å, Fig. 3 *C* and *F*). All fibrils have a width at crossover of ~37 Å and thus a nearly rectangular cross-section (Fig. 3 *D*–*F*). The widths between crossovers correspond to integer multiples of the peptide chain length (~38 Å × 2, 3, or 4) and indicate the presence of multiple protofilaments (11, 19).

The internal packing of the protofilaments is revealed by examination of cross-sections through the 3D fibril reconstructions. Although the three fibril morphologies differ in the dimensions of the long side of their cross-sections (Fig. 3 *D*–*F*), they are remarkably similar in other respects. In particular, they are all composed of two elongated, high-density regions separated by a well-defined region of low density (~13 Å wide at 1σ above the mean density) that extends to the slightly open cross-sectional ends (Fig. 3 *D*–*F*). The high-density regions are ~12 Å in width (at 1σ above the mean density) and correspond to the paired β-sheets of individual protofilaments (11, 12, 16, 19) arranged in a linear fashion. The electron density maps all display twofold symmetry (Fig. 3 *D*–*F*), which was not imposed during image processing, about the long axis of the fibril. This axial symmetry relates the paired β-sheet density regions to each other so that all of the fibrils described here are left-handed, double-layered helical ribbons with a hollow core (Fig. 3 *A*–*F*).
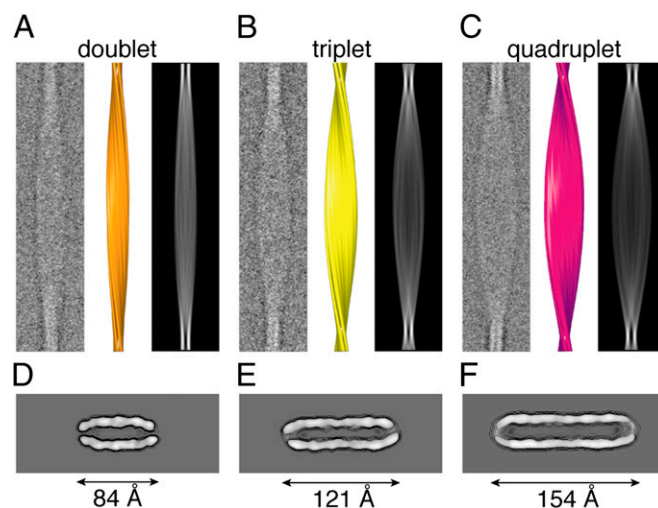

Fig. 3. Representative cryo-EM images of averaged fibrils (class averages), surface representations of reconstructions, 2D projections, and contoured density cross-sections of the three types of fibril formed by TTR(105–115). (*A*) Doublet class average (*Left*), 3D reconstruction (*Center*; orange), and 2D projection of the fibril reconstruction (*Right*). (*B*) Triplet class average (*Left*), 3D reconstruction (*Center*; yellow), and 2D projection of the fibril reconstruction (*Right*). (*C*) Quadruplet class average (*Left*), 3D reconstruction (*Center*; purple), and 2D projection of the fibril reconstruction (*Right*). (*D*–*F*) Contoured density cross-sections of the doublet (*D*), triplet (*E*), and quadruplet (*F*) fibrils. Contours represent density levels of multiples of 0.5σ above the average density of the background (outermost contour). Measurements of dimensions were determined at 1.0σ above the mean density.

Because the cryo-EM maps strongly suggest that the fibrils formed by TTR(105–115) are composed of integer multiples of linearly connected protofilaments, we sought to identify the inter-protofilament packing interface. Low-angle X-ray experiments on TTR(105–115) fibrils (34) indicate an equatorial repeat of 37 ± 2 Å, which closely matches the length of the TTR(105–115) peptide in an extended β-strand conformation (38 Å; Fig. 2A); this observation suggests that the protofilaments are stacked in a periodic manner in the peptide chain direction. We therefore isotopically labeled the termini of the peptide (^{15}N–Y105 and ^{13}CO–S115) and performed rotational-echo double-resonance (REDOR) (35) experiments to probe for backbone-to-backbone contacts. The observation of a strong dipolar coupling between S115–^{13}CO$_2$–^{15}NH$_3^+$–Y105, corresponding to an interprotofilament distance of 3.57 ± 0.06 Å, indicates the presence of head-to-tail contacts between adjacent protofilaments (Fig. 1D). This result is crucial in determining the relative orientations of individual protofilaments within the overall fibril topology (Fig. 1D).

The head-to-tail, interprotofilament packing interface (Fig. 2C) is very closely matched (shape complementarity = 0.83) and appears to be stabilized by dipole–dipole interactions between the N and C termini of peptide chains in neighboring protofilaments (SI Appendix, Fig. S7) and by four hydrogen bonds between the terminal C=O and N–H groups (Fig. 2C) and two tyrosine (OH...O) hydrogen bonds (Fig. 2C).

Atomic-Level Structures of the Fibril Polymorphs. The reconstructed cross-sectional density maps are fully consistent with the NMR-derived protofilament structure discussed above (SI Appendix, Fig. S8) and can accommodate perfectly four, six, or eight of the two-sheet protofilaments interconnected in a head-to-tail fashion (Fig. 4 A–C). Side-chain details are only present in exceptionally high-resolution electron density maps (3.3–4 Å) (36), which is not the case here because the resolution of the three maps is ~11 Å (SI Appendix, Table S4 and Fig. S9). As a result of the slightly curved cross-section of the protofilaments (Fig. 2C), the presence of a twofold symmetry axis (Fig. 3 D–F), and the nanometer resolution (SI Appendix, Table S4) of the 3D reconstructions, there is a common structural arrangement that gives the best fit to the set of electron density maps (up to 7% less atoms outside the electron density maps at 1.0σ threshold) and on average more than seven times more interfacial contact area (with no steric clashes; Fig. 4 D–F) than other alternative structures. This structural arrangement involves a pair of oppositely directed, linear stretches of two (Fig. 4A and SI Appendix, Fig. S10A and Table S3), three (Fig. 4B and SI Appendix, Fig. S10B and Table S3) and four (Fig. 4C and SI Appendix, Fig. S10C and Table S3) protofilaments with the even-numbered residues (TALSY) lining the outer surface of the fibrils and the odd-numbered residues (YIALPS) buried in the hollow core (Fig. 4 D–F). Therefore, different numbers of otherwise identical protofilaments (12) are able to self-assemble into a generic structural arrangement.

To obtain an independent estimate of the number of peptides contained in the fibril cross-sections, we performed STEM mass-per-length (MPL) measurements on an ensemble of fibrils (Fig. 5A). The distribution can be described by three Gaussian curves peaking at 9.7 ± 1.2, 12.8 ± 1.2, and 15.9 ± 1.2 peptides per 4.67-Å layer of the different types of fibril. These MPL measurements are in good agreement with the cryo-EM fibril reconstructions (Fig. 4 A–C), which have cross-sections with twofold symmetry (Fig. 3 D–F) able to accommodate 8 (Fig. 4A), 12 (Fig. 4B), or 16 (Fig. 4C) peptides—i.e., 4, 6, or 8 two-sheet protofilaments—respectively. As an additional validation, we simulated the X-ray diffraction pattern of the fibril cross-sections and found that the resulting peaks closely match the primary and secondary reflections in the experimental diffraction pattern (34) (Fig. 5B).

The cryo-EM maps of the three fibrils are characterized by a nearly constant ~16-Å backbone-to-backbone low-density region between the high-density regions of paired β-sheets (Figs. 3 D–F and 4 A–C). Such a separation suggests that this interface may contain structured water involved in a hydrogen-bonded network with the exposed side chains (Fig. 4 D–F) and water molecules. The dimensions of the cavity (Figs. 3 D–F and 4 A–C) can accommodate the two sets of exposed β-sheet side chains (~9 Å), leaving a 2×3.4 Å (the diameter of a water molecule) ~7 Å layer for water molecules to occupy (Fig. 4 D–F). Moreover, the cavity dimension matches very closely the size of the wet interfaces in amyloid-like microcrystals in which crystal contacts result in a bilayer of water molecules that can be observed crystallographically (21). Molecular dynamics simulations (SI Appendix, SI Materials and Methods) suggest that a single layer of water molecules becomes bound to each of the slightly hydrophilic protofilament surfaces (SI Appendix, Fig. S11).

Extensive AFM imaging, which has a much higher contrast than single cryo-EM images, of TTR(105–115) samples (Fig. 5C) revealed the presence of a low population (~3% of the total fibril dataset) of singlet fibrils, or "filaments," with a uniform height of 38.7 ± 4.4 Å (Fig. 5C). The dimensions of this species match perfectly the predicted height profile of a pair of protofilaments separated by the constant ~16 Å (backbone to backbone) water cavity (overall dimensions 38×43 Å; SI Appendix, Fig. S12). We also saw no evidence of the number of protofilaments per fibril varying along the length of a single TTR(105–115) fibril (37). Rather, it is clear from the cryo-EM images (Fig. 3) and 3D reconstructions (Fig. 4), AFM images, and STEM MPL measurements of TTR(105–115) fibrils (Fig. 5) that there are three main subsets of the fibril population—namely, the doublet, triplet, and quadruplet fibrils (Fig. 6 and SI Appendix, Figs. S13–S15).

To determine the complete structures of the amyloid fibrils (Fig. 6, SI Appendix, Figs. S13–S15, and Movies S2, S3, and S4), a helical symmetry was imposed on to the NMR/cryo-EM atomic cross-sections to generate longer fibril segments (Fig. 6, SI Appendix, Figs. S13–S15, and Movies S2, S3, and S4). The fit of four,
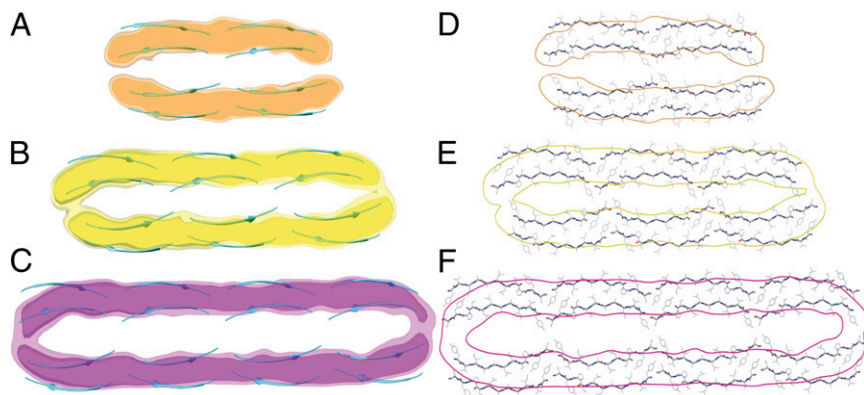
Fig. 4. Atomic-resolution cross-sections of the three types of TTR(105–115) amyloid fibrils determined by combining MAS NMR and cryo-EM. Reconstructed cross-section density maps are shown as two electron density isosurfaces (1.0σ and 2.2σ above the mean density) with the secondary structure of the constituent NMR-derived protofilaments shown in a cyan ribbon representation. (A–C) The doublet (A), triplet (B), and quadruplet (C) fibril cross-sections can accommodate pairs of two, three, and four interconnected protofilaments, respectively. (D–F) All-atom representation of the doublet (D), triplet (E), and quadruplet (F) cross-sections with cryo-EM envelopes superimposed. Cryo-EM envelopes are shown as orange, yellow, and purple contours at 1.0σ above the mean density for doublet, triplet, and quadruplet fibrils, respectively. For a discussion on the resolution of the cryo-EM maps, see SI Appendix, Table S4.
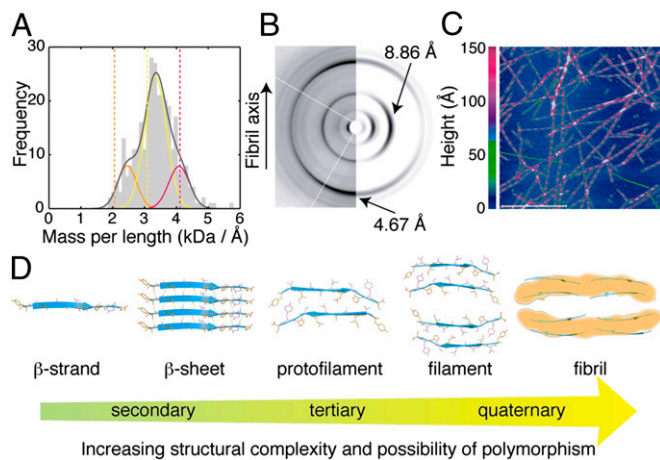
Fig. 5. Five diverse biophysical techniques were integrated to determine unambiguously the structures of each of the motifs that make up the TTR (105–115) amyloid fibrils. Spanning five orders of magnitude, the overlapping length scales of MAS NMR (0.1–10 Å), X-ray diffraction (3–100 Å), cryo-EM (8–1,000 Å), AFM (30–1,000 Å), and STEM (80–1,000 Å) enabled us to derive self-consistent, high-precision structural restraints on the secondary (β-strand and -sheet; distance restraints of <6 Å), tertiary (protofilament; distance restraints of 4.5–37 Å), and quaternary structure (filament and fibril; distance restraints of 16–1,000 Å) of the TTR(105–115) amyloid fibrils. (*A*) Histogram of STEM MPL measurements of TTR(105–115) fibrils, which reveals three populations of fibrils, with a best fit (gray solid line) being the sum of three Gaussian curves with values of 2.5 ± 0.3 kDa/Å (orange solid line), 3.3 ± 0.3 kDa/Å (yellow solid line), and 4.1 ± 0.3 kDa/Å (purple solid line). The orange, yellow, and purple dashed lines refer to the number of TTR(105–115) peptides per 4.67-Å repeat in the doublet (8 peptides), triplet (12 peptides), and quadruplet (16 peptides) fibrils, respectively. (*B*) Comparison of the high-resolution experimental X-ray diffraction pattern from TTR(105–115) fibrils (34) (*Left*) and the simulated X-ray diffraction pattern for TTR(105–115) fibrils (*Right*). The fibril axis is vertical, with the incident beam directed orthogonally to this axis. The meridional reflection at 4.67 Å and the equatorial reflection at 8.86 Å are characteristic of cross-β structure. (*C*) High-resolution AFM image of fibrils (pink and purple) and filaments (green) formed by TTR (105–115). (Scale bar, 1 μm.) Fibrils (pink and purple) have heights ranging from 70 to 160 Å and pitches of 950 ± 100 Å. The filament has an average height of 38.7 ± 4.4 Å. (*D*) Hierarchy of atomic-resolution motifs involved in the self-assembly of the amyloid fibrils and their polymorphism.

six, and eight protofilament structures winding around a hollow core to the doublet, triplet, and quadruplet fibril densities is excellent with correlation coefficients of 0.85, 0.88, and 0.86, respectively (Fig. 6, *SI Appendix*, Figs. S13–S15, and Movies S2, S3, and S4). These structures have a rmsd of the backbone and all heavy atoms in the ensemble of the 20 lowest energy conformers of 0.4, 0.6, 0.6 Å and 0.6, 0.7, 0.7 Å, respectively (*SI Appendix, Table S3 and Fig. S10*). None of the structures has any residue with torsion angles in disallowed regions of the Ramachandran plot (*SI Appendix, Table S3*).

These results indicate that, in analogy to microtubules (38), interprotofilament interactions are highly conserved across different types of filamentous structures. However, because the termini of the β-sheets are involved in the higher-order assembly, the lateral association of two or more protofilaments occludes the hydrophilic surfaces so that the proportion of exposed hydrophobic surface area increases steeply with increasing fibril diameter. Because the fibrils have a large fraction of exposed hydrophobic residues (up to 23% more than typical globular proteins), this free energy penalty may be offset by the stabilization arising from the highly optimal packing that allows extensive backbone hydrogen bonding (39). The specific head-to-tail electrostatic interactions between protofilaments that we have identified (Fig. 2*C* and *SI Appendix*, Fig. S7) indicate how these elements can self-associate under one set of chemical conditions into three highly populated and distinct ultrastructural

polymorphs, with varying widths and pitches that are propagated over many microns (4) (Fig. 6, *SI Appendix*, Figs. S13–S15, and Movies S2, S3, and S4).

Discussion

An atomic-resolution structure of a cross-β amyloid fibril and its constituent self-assembling subunits has proved elusive to structural biology. Such a structure is of great interest, because the thermodynamic and kinetic properties of amyloid fibrils, as well as their frequently adverse effects on cellular homeostasis leading to disease, are linked to the details of their morphological features (40). In this study, we have resolved each of the structural elements in a cross-β amyloid fibril to atomic resolution, thus revealing the structural basis for the hierarchical organization of these aggregates. The architecture of the fully assembled amyloid fibrils is not strongly dependent on sequence because the constituent β-strands within the core of the fibril are linked by a vast array of interbackbone hydrogen bonds (Fig. 2*A* and Movie S1), which are main-chain interactions common to all polypeptides (23). This generic character is evident in the marked similarity in appearance (17), dimensions (12), X-ray diffraction patterns (3), material properties (5), kinetics (31), thermodynamic stabilities (6), and dye-binding properties (41) of fibrils formed by peptides and proteins varying widely in sequence and native conformation.

The nature of the side-chains does, however, modulate the details of the fibrillar scaffold by determining which regions of the sequence self-associate to form the intermolecular packing arrangement within, and between, the constituent β-sheets of the fibril core (1, 2). Although side chains influence which protofilament structures are adopted under a given set of experimental conditions, ultrastructural polymorphism is also a common feature of amyloid fibrils (1, 2). This variability at the intra- and interprotofilament levels provides an explanation of different fibril polymorphs characteristic of distinct clinical subphenotypes, in analogy to the strains of prions (42).

The ability to understand the hierarchical organization of cross-β amyloid fibrils (Fig. 5*D*) reveals how this structure
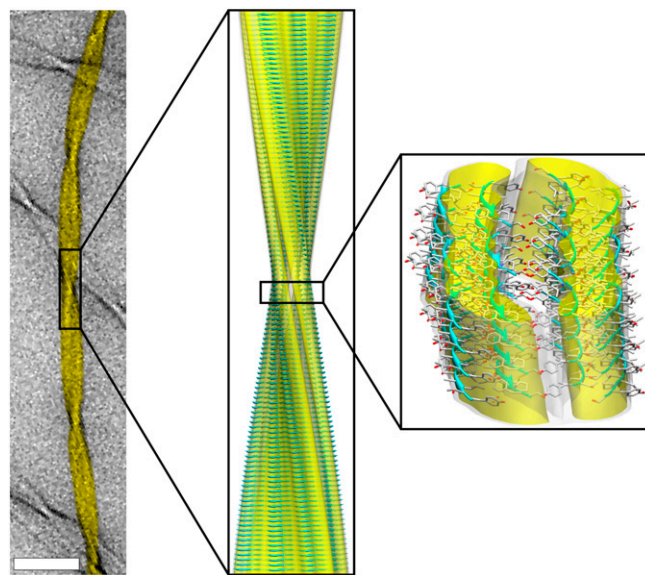

Fig. 6. Close-up view of the MAS NMR atomic-resolution structure of the triplet fibril fitted into the cryo-EM reconstruction (*Center*). The background image of the fibril (*Left*) was taken using TEM. (Scale bar, 50 nm.) The fibril surfaces (*Right*) are shown at 1.0σ (white) and 2.2σ (yellow) above the mean density, respectively, and the constituent β-sheets are shown in a ribbon representation; oxygen, carbon, and nitrogen atoms are shown in red, gray, and blue, respectively.

represents a template that many amino acid sequences can adopt (23). Thus, although in longer sequences additional residues will undoubtedly affect the overall assembly of the fibrils and the nature of interactions between protofilaments (11), the basic structural elements (Fig. 5D) remain closely similar (12, 17, 43). In this respect, understanding the formation and molecular pathology of the cross-β fibrils formed by other peptides and proteins involves the study of variations on a theme common to most polypeptide chains (23). Indeed, both polar and nonpolar (22), and even homopolymeric (44) sequences can adopt the cross-β form of polypeptide states. By contrast, the β-helical structure of HET-s(218-289) fibrils (18) which represents a functional yeast prion, is stabilized by specific interactions selected through evolution and therefore not accessible to most amino acid sequences. The structures presented here (Fig. 6, *SI Appendix*, Figs. S13–S15, and Movies S2, S3, and S4) have instead the widely accessible cross-β geometry commonly associated with misfolding disorders such as Alzheimer's disease and type II diabetes (1, 2).

Conclusions

We have determined the atomic-resolution structure of a cross-β amyloid fibril and two of its associated polymorphic variants. Our approach has enabled us to dissect each distinct level of the structural hierarchy of the fibrils at atomic resolution and to identify the packing interactions that drive the self-assembly and ultimately stabilize these persistent filamentous aggregates. The results that we have presented illustrate the increasing potential for amyloid polymorphism with the ascending hierarchy of fibrillar structures, a phenomenon that we expect to be common for many other peptides and proteins.

Methods

Amyloid fibrils were prepared by dissolving TTR(105–115) in a 10% (vol/vol) acetonitrile/water solution (adjusted to pH 2 with HCl) at a concentration of 15 mg/mL. The samples were incubated for 2 d at 37 °C followed by incubation for 14 d at room temperature (20). The samples were routinely characterized by TEM, and great care was taken to ensure that the morphologies of the fibrils studied by NMR were identical to those examined by cryo-EM and the other techniques (X-ray diffraction, AFM, and STEM).

Full methods are available as *SI Appendix, SI Materials and Methods*.

1. Chiti F, Dobson CM (2006) Protein misfolding, functional amyloid, and human disease. *Annu Rev Biochem* 75:333–366.
2. Eisenberg D, Jucker M (2012) The amyloid state of proteins in human diseases. *Cell* 148(6):1188–1203.
3. Sunde M, et al. (1997) Common core structure of amyloid fibrils by synchrotron X-ray diffraction. *J Mol Biol* 273(3):729–739.
4. Knowles TPJ, Smith JF, Craig A, Dobson CM, Welland ME (2006) Spatial persistence of angular correlations in amyloid fibrils. *Phys Rev Lett* 96(23):238301.
5. Knowles TP, et al. (2007) Role of intermolecular forces in defining material properties of protein nanofibrils. *Science* 318(5858):1900–1903.
6. Baldwin AJ, et al. (2011) Metastability of native proteins and the phenomenon of amyloid formation. *J Am Chem Soc* 133(36):14160–14163.
7. Hartl FU, Bracher A, Hayer-Hartl M (2011) Molecular chaperones in protein folding and proteostasis. *Nature* 475(7356):324–332.
8. Fowler DM, Koulov AV, Balch WE, Kelly JW (2007) Functional amyloid—from bacteria to humans. *Trends Biochem Sci* 32(5):217–224.
9. Haass C, Selkoe DJ (2007) Soluble protein oligomers in neurodegeneration: Lessons from the Alzheimer's amyloid beta-peptide. *Nat Rev Mol Cell Biol* 8(2):101–112.
10. Gazit E (2002) A possible role for pi-stacking in the self-assembly of amyloid fibrils. *FASEB J* 16(1):77–83.
11. Jiménez JL, et al. (1999) Cryo-electron microscopy structure of an SH3 amyloid fibril and model of the molecular packing. *EMBO J* 18(4):815–821.
12. Jiménez JL, et al. (2002) The protofilament structure of insulin amyloid fibrils. *Proc Natl Acad Sci USA* 99(14):9196–9201.
13. Lührs T, et al. (2005) 3D structure of Alzheimer's amyloid-beta(1-42) fibrils. *Proc Natl Acad Sci USA* 102(48):17342–17347.
14. Petkova AT, et al. (2002) A structural model for Alzheimer's beta-amyloid fibrils based on experimental constraints from solid state NMR. *Proc Natl Acad Sci USA* 99(26):16742–16747.
15. Petkova AT, et al. (2005) Self-propagating, molecular-level polymorphism in Alzheimer's beta-amyloid fibrils. *Science* 307(5707):262–265.
16. Sachse C, Fändrich M, Grigorieff N (2008) Paired beta-sheet structure of an Abeta(1-40) amyloid fibril revealed by electron microscopy. *Proc Natl Acad Sci USA* 105(21):7462–7466.
17. Schmidt M, et al. (2009) Comparison of Alzheimer Abeta(1-40) and Abeta(1-42) amyloid fibrils reveals similar protofilament structures. *Proc Natl Acad Sci USA* 106(47):19813–19818.
18. Wasmer C, et al. (2008) Amyloid fibrils of the HET-s(218-289) prion form a beta solenoid with a triangular hydrophobic core. *Science* 319(5869):1523–1526.
19. Zhang R, et al. (2009) Interprotofilament interactions between Alzheimer's Abeta1-42 peptides in amyloid fibrils revealed by cryoEM. *Proc Natl Acad Sci USA* 106(12):4653–4658.
20. Jaroniec CP, et al. (2004) High-resolution molecular structure of a peptide in an amyloid fibril determined by magic angle spinning NMR spectroscopy. *Proc Natl Acad Sci USA* 101(3):711–716.
21. Nelson R, et al. (2005) Structure of the cross-beta spine of amyloid-like fibrils. *Nature* 435(7043):773–778.
22. Sawaya MR, et al. (2007) Atomic structures of amyloid cross-beta spines reveal varied steric zippers. *Nature* 447(7143):453–457.
23. Dobson CM (1999) Protein misfolding, evolution and disease. *Trends Biochem Sci* 24(9):329–332.
24. Caporini MA, et al. (2010) Accurate determination of interstrand distances and alignment in amyloid fibrils by magic angle spinning NMR. *J Phys Chem B* 114(42):13555–13561.
25. Jaroniec CP, Filip C, Griffin RG (2002) 3D TEDOR NMR experiments for the simultaneous measurement of multiple carbon-nitrogen distances in uniformly (13)C,(15)N-labeled solids. *J Am Chem Soc* 124(36):10728–10742.
26. Ladizhansky V, Griffin RG (2004) Band-selective carbonyl to aliphatic side chain 13C-13C distance measurements in U-13C,15N-labeled solid peptides by magic angle spinning NMR. *J Am Chem Soc* 126(3):948–958.
27. Szeverenyi NM, Sullivan MJ, Maciel GE (1982) Observation of spin exchange by two-dimensional fourier-transform C-13 cross polarization-magic-angle spinning. *J Magn Reson* 47:462–475.
28. Sivanandam VN, et al. (2011) The aggregation-enhancing huntingtin N-terminus is helical in amyloid fibrils. *J Am Chem Soc* 133(12):4558–4566.
29. Schneider R, et al. (2011) Structural characterization of polyglutamine fibrils by solid-state NMR spectroscopy. *J Mol Biol* 412(1):121–136.
30. Collins SR, Douglass A, Vale RD, Weissman JS (2004) Mechanism of prion propagation: Amyloid growth occurs by monomer addition. *PLoS Biol* 2(10):e321.
31. Knowles TPJ, et al. (2009) An analytical solution to the kinetics of breakable filament assembly. *Science* 326(5959):1533–1537.
32. Goldsbury CS, et al. (2000) Studies on the in vitro assembly of a beta 1-40: Implications for the search for a beta fibril formation inhibitors. *J Struct Biol* 130(2-3):217–231.
33. Goldsbury CS, et al. (1997) Polymorphic fibrillar assembly of human amylin. *J Struct Biol* 119(1):17–27.
34. Gras SL, et al. (2008) Functionalised amyloid fibrils for roles in cell adhesion. *Biomaterials* 29(11):1553–1562.
35. Gullion T, Schaefer J (1989) Rotational-echo double-resonance NMR. *J Magn Reson* 81:196–200.
36. Orlova EV, Saibil HR (2011) Structural analysis of macromolecular assemblies by electron microscopy. *Chem Rev* 111(12):7710–7748.
37. Komatsu H, Feingold-Link E, Sharp KA, Rastogi T, Axelsen PH (2010) Intrinsic linear heterogeneity of amyloid β protein fibrils revealed by higher resolution mass-per-length determinations. *J Biol Chem* 285(53):41843–41851.
38. Sui HX, Downing KH (2010) Structural basis of interprotofilament interaction and lateral deformation of microtubules. *Structure* 18(8):1022–1031.
39. Fitzpatrick AW, Knowles TPJ, Waudby CA, Vendruscolo M, Dobson CM (2011) Inversion of the balance between hydrophobic and hydrogen bonding interactions in protein folding and aggregation. *PLoS Comp Biol* 7(10):e1002169.
40. Vendruscolo M, Knowles TPJ, Dobson CM (2011) Protein solubility and protein homeostasis: A generic view of protein misfolding disorders. *Cold Spring Harb Perspect Biol* 3(12):3.
41. Krebs MRH, Bromley EHC, Donald AM (2005) The binding of thioflavin-T to amyloid fibrils: Localisation and implications. *J Struct Biol* 149(1):30–37.
42. Collinge J, Clarke AR (2007) A general model of prion strains and their pathogenicity. *Science* 318(5852):930–936.
43. Bayro MJ, et al. (2011) Intermolecular structure determination of amyloid fibrils with magic-angle spinning and dynamic nuclear polarization NMR. *J Am Chem Soc* 133(35):13967–13974.
44. Fändrich M, Dobson CM (2002) The behaviour of polyamino acids reveals an inverse side chain effect in amyloid structure formation. *EMBO J* 21(21):5682–5690.

BIOCHEMISTRY

Atomic structure and hierarchical assembly
of a cross-β amyloid fibril

Materials and Methods

Sample Preparation:

Transthyretin(105-115), or TTR(105-115), was synthesized using solid-phase methods and purified by HPLC (CS Bio, Menlo Park, CA and New England Peptide, Gardner, MA). The isotopically labeled amino acids for the synthesis were purchased from Cambridge Isotope Laboratories, Andover, MA. The following labeling schemes were used (labeled residues are shown as bold and underlined): uniformly ^{15}N, ^{13}C **YTIA**ALL**SPY**S; uniformly ^{15}N, ^{13}C YTI**AALL**SPYS; and a sample labeled with ^{15}N at Y105, and ^{13}C at the S115 carbonyl position. Amyloid fibrils were prepared by dissolving ~ 15 mg peptide/mL in a 10% v/v acetonitrile/H_2O solution, adjusted to pH 2.0 with HCl. The solution was incubated at 37 °C for 2 days, followed by 14 days at 25 °C. After this period, the mature fibrils were characterized by TEM and great care was taken to ensure that the morphology of the fibrils studied by NMR was identical to those examined by cryo-EM and the other techniques (X-ray diffraction, AFM and STEM). The viscous gel containing the mature fibrils was transferred to a centrifuge tube and washed twice with 2 ml of 10% v/v acetonitrile/water at pH 2. After each wash the sample was centrifuged for 2 h at 4°C and 320,000 x g. After the second spin 10-15 mg of the pellet were packed into either into a 4 mm zirconia rotor (20 mg fibrils, Varian-Agilent Technologies, Santa Clara, CA) or a 3.2 mm rotor (15 mg of fibrils, Bruker BioSpin, Billerica, MA).

MAS NMR Experiments:

1D DQ-DRAWS (1, 2) and REDOR (3) experiments were performed on a custom-built spectrometer (courtesy of D. J. Ruben, Francis Bitter Magnet Laboratory, Massachusetts Institute of Technology, Cambridge, MA) operating at 500 MHz ^{1}H Larmor frequency, and equipped with a 4 mm ^{1}H/^{13}C/^{15}N Varian-Chemagnetix probe (Varian, Inc., Palo Alto, CA). The sample used for these experiments was labeled in the following way: ^{15}N-Y105, ^{13}C$_1$-S115. REDOR experiments were performed at 9 kHz MAS, with 50 kHz ^{15}N pulses, 100 kHz ^{13}C pulses, and 100 kHz TPPM decoupling during mixing and acquisition. 640 scans were acquired at each mixing time, for both S and S_o experiments, with a scan delay of 3.0 s.

DQ-DRAWS distances for I107, A108, A109, L110, L111, S112, and P113 carbonyl atoms were previously published in Ref. 1. In this work, we report the DQ-DRAWS distance for S115. This experiment was performed at 6.534 kHz MAS, utilizing 55 kHz ^{13}C pulses, 100 kHz ^{1}H continuous-wave decoupling during mixing, and 100 kHz TPPM decoupling (4) during acquisition. 6650 scans were acquired at each mixing time, with a scan delay of 3.0 s.

The experiments on the YTI**AALL**SPYS sample were performed on a custom-built 500 MHz spectrometer (courtesy of D. J. Ruben, Francis Bitter Magnet Laboratory, Massachusetts Institute of Technology, Cambridge, MA) equipped with a 4 mm triple channel Varian-Chemagnetix probe. ZF-TEDOR experiments were performed with 83 kHz ^{1}H TPPM decoupling, 83 kHz ^{13}C pulses and 50 kHz ^{15}N pulses during mixing. R2TRW experiments were performed as described in Ref. (5), with 25 ms mixing, 83 kHz TPPM decoupling, and a carrier frequency set at 65 ppm. The spinning frequency was set to 10.1 kHz.

2D PDSD (6) experiments were performed on a Bruker spectrometer operating at 900 MHz [1]H Larmor frequency, equipped with a triple-channel 3.2 mm E-free MAS probe (Bruker BioSpin, Billerica, MA). The sample used for these experiments was prepared by mixing U-^{13}C, ^{15}N labeled **YTIA**ALLSPYS, and U-^{13}C, ^{15}N labeled YTIAALL**SPY**S in a 1:1 ratio before fibrilization. The experiments were performed at 11 kHz MAS, with mixing times of 50 ms, 100 ms, 200 ms and 300 ms, and 83 kHz TPPM decoupling during acquisition. 32 scans were recorded per t_1 point (892 t_1 points, 11.5 ms t_1 evolution and 24 ms t_2 evolution).

ZF-TEDOR (7) experiments were performed using the same sample on a custom-built spectrometer (courtesy of D. J. Ruben, Francis Bitter Magnet Laboratory, Massachusetts Institute of Technology, Cambridge, MA) operating at 750 MHz [1]H Larmor frequency, and utilizing a triple-channel 3.2 mm Bruker E-free MAS probe (Bruker BioSpin, Billerica, MA). 40 kHz ^{15}N pulses, 83 kHz ^{13}C pulses, and 91 kHz ^{1}H TPPM decoupling during mixing and acquisition were used in this case, while $\omega_r/2\pi = 12.5$ kHz. Experiments with $\tau_{mix} = 4.80$ ms, 5.44 ms, 6.08 ms, 7.04 ms, 7.64 ms, 8.64 ms, 9.60 ms, 10.24 ms, 11.84 ms, 13.44 ms, and 15.04 ms were acquired, with 128 scans per t_1 point, per experiment. In total, 256 t_1 points were collected, with 10.2 ms t_1 acquisition, and 24 ms t_2 acquisition, and 2.7 s scan delay.

The temperature of the cooling gas in each case was set to 2 ºC, while we estimate that the actual sample temperature was 10-15 ºC, depending on $\omega_r/2\pi$ and rf-induced heating. Spectra were processed and analyzed using the programs NMRPipe (8) and Sparky (9). Indirect external referencing to DSS was done based on adamantane ^{13}C chemical shifts (10).

MAS NMR Data Fitting:
Distances were extracted from buildup curves (DQ-DRAWS, TEDOR) and dephasing curves (REDOR) using the SPINEVOLUTION simulation program (11). The DQ-DRAWS data was fit as described previously in Ref. (1), while a detailed description of the simulation of REDOR spectra with SPINEVOLUTION is given in Ref. (11). In all cases, the error in the reported distances was based on the 95% confidence interval derived from the elements of the covariance matrix of the fit.

TEDOR simulations were performed in the following way: The Ala108 spin system was approximated by a ^{15}N atom and two ^{13}C atoms, corresponding to Cα and Cβ, with $J_{C\alpha-C\beta} = 20$ Hz also included in the simulation. For the simulation of the relevant longer distances, a second ^{15}N atom was included in the spin system, corresponding to Ser112N or P113N. A relaxation parameter and the distance between Ala108Cβ and the distant ^{15}N were used as fit parameters in the simulation. The Ile107 spin system was approximated by a ^{15}N atom and four ^{13}C atoms

(corresponding to Cβ, Cγ2, Cγ1, and Cδ1). The J-coupling between Cδ1 and Cγ2 was set to 20 Hz.

The TEDOR distances were used to calibrate three different constraint classes (2.5-4.5 Å -> 100 ms, 2.5-6.5 Å ->200 ms, 2.5-8.5 Å -> 400 ms) for the PDSD spectra with each contact assigned to a distance class depending upon the mixing time at which the cross-peak first appeared.

Structure Calculations:
Structure calculations of the protofilament, doublet, triplet and quadruplet fibril structures were performed using CNSsolve version 1.1 (12) by applying the molecular dynamics simulated annealing protocol with torsion angles as internal degrees of freedom. Structures were constructed in a hierarchical fashion. First, the structure of a single β-sheet composed of 8 β-strands was solved using only the intra-molecular distance and dihedral angle restraints (13) and the intra-sheet restraints (Table S1). Then, the structure of a two-sheet protofilament (with 8 β-strands per β-sheet) was determined using the intra-molecular distance and dihedral angle restraints (13), the intra-sheet restraints (Table S1) and the inter-sheet restraints (Table S2) and the single β-sheet structure as the starting point for the calculation. Finally, the doublet, triplet and quadruplet fibril structures (with 8 β-strands per β-sheet) were determined by using the intra-molecular distance and dihedral angle restraints (13), the intra-sheet restraints (Table S1), the inter-sheet restraints (Table S2) and the inter-protofilament restraints (distance between S115-$^{13}CO_2^-$--$^{15}NH_3^+$-Y105 is 3.57±0.06 Å) and the protofilament structure as the starting point for the calculation. The annealing protocol consisted of high-temperature molecular dynamics at 20,000 K for a total of 50,000 steps with 3 ps per step, followed by two cooling stages, where the temperature was first gradually decreased from 20,000 K to 1000 K in 200,000 steps and then from 1,000 K to 50 K in 200,000 steps. In addition to the experimental distance and dihedral angle restraints, which were modeled with square well-quadratic potentials, the total energy target function included energy terms representing covalent bonds, three-atom bond angles and dihedral (improper) angles required to maintain correct geometries, and van der Waals interactions (12). Since the monomer structure was accurately determined (13), the non-crystallographic symmetry (NCS) term was also included and maintained at the weight k_{NCS}=2 kcal/mol throughout the protocol (14). A family of 100 lowest energy conformers was generated for the protofilament, doublet, triplet and quadruplet structures. The lowest energy structure from the calculation was used to represent the ensemble. The final structures had no experimental distance violations >0.3 Å or dihedral angle violations >5°. The Ramachandran statistics were generated using PROCHECK (15) and show that no residue of the lowest energy structure adopts disallowed conformations regarding φ and/or ψ dihedral angles.

Cryo-EM and 3D reconstruction:

All fibril specimens were stored at 4°C. For cryo-EM imaging, fibrils were applied to holey carbon films (R2/2, QuantifoilMicro Tools GmbH, Jena, Germany) that were immediately plunge-frozen at liquid nitrogen temperature. The cryo grids were maintained at –174 °C in a Gatan 626 cryo-holder. Low-dose images of amyloid fibrils formed by the TTR(105-115) molecules were taken on a Tecnai F20 electron microscope (FEI, Netherlands) operated at 200 keV. Images were recorded on Kodak SO-163 film at 40,000x nominal magnification and a defocus range between 0.9 and 3.0 μm underfocus. Micrographs were digitized on a Zeiss SCAI

microdensitometer (Z/I Imaging) with a step size of 7 μm corresponding to a pixel size of 1.8 Å at specimen level.

EM images of fibrils embedded in vitreous ice were analysed by a combined helical and single particle approach (16, 17). Approximately 4,000 images of fibrils that included two crossovers were selected manually and corrected for the effects of the contrast transfer function of the microscope using CTFFIND3 (18), and band-pass filtered and normalized using SPIDER (19).

The alignment determined for each segment was then applied and subjected to multivariate statistical analysis (MSA) in IMAGIC (20). Fibrils were sorted first on the basis of width and then according to helical pitch by examining the main eigenimages from the multivariate statistical analysis. In subsequent rounds of classification, in addition to examining the main eigenimages, width discrimination was refined by taking the autocorrelation of the line profile of the widest (central) part of the fibrils using a very small number of superimposed images (~5 images per set). In this way, we were able to separate out more accurately the different types of fibril into homogeneous, separate groups (classes) even at very low signal:noise. Fibril classes were then computationally segmented into a series of small boxes (120x120 pixels) with 86% overlap, which were used as input views for helical reconstruction (21). The pitch was determined from the cross-over separation using auto-correlation and structures for each width class were treated as continuous helices to reconstruct short segments. Iterative rounds of projection matching of these fibril segments to 3D fibril models from the best classes improved the Euler angles of successive 3D reconstructions resulting in final electron density maps with nanometer resolution (Table S4). Reconstructions were calculated using the BKRP program (22).

Fitting of NMR structures to cryo-EM fibril maps:
NMR figures were prepared in PyMOL using the program's hydrogen bond geometric criteria to identify all possible hydrogen bonds within the (.pdb) structures. All fittings were performed analytically using the Chimera program (23). The fit quality has been assessed by maximizing cross-correlation between atomic models and the electron density of EM structures when the resolution of the models was adjusted to the resolution of the EM maps. The resulting best fits were rendered in Chimera (23).

STEM Mass-per-length (MPL) measurements:
STEM mass-per-length (MPL) measurements were performed on an ensemble of fibrils using a Vacuum Generators HB-5 scanning transmission microscope (STEM) operated at 80 kV. MPL data were calibrated using Tobacco Mosaic Virus (TMV). We present a best fit of three Gaussian curves to the MPL histogram.

The amyloid fibrils prepared by dissolving TTR(105-115) in a 10% v/v acetonitrile/water solution (adjusted to pH2 with HCl) at 10 mg/ml were examined. The stock was diluted 67x in water or 50x in 10% v/v acetonitrile/water. 4 μl aliquots were then adsorbed for 1 min to glow-discharged thin carbon films supported on holey carbon films on 200-mesh gold-plated copper grids. The grids were blotted, washed on 6 or 10 drops of quartz double-distilled water, respectively, and plunge-frozen in liquid nitrogen. They were freeze-dried in two separate runs at -80 °C and 5×10^{-8} Torr overnight in the microscope. Tobacco mosaic virus (kindly supplied by Dr. R. Diaz-Avalos, Institute of Molecular Biophysics, Florida State University) adsorbed to a separate grid, washed with 100mM ammonium acetate and air-dried, served as mass standard.

Images (512x512 pixel) were recorded using a Vacuum Generators HB-5 STEM interfaced to a modular computer system (Tietz Video and Image Processing Systems GmbH, D-8035 Gauting, Germany) at 80 kV and a nominal magnification of 200,000x. The average imaging dose was 360 ± 45 e/nm^2. Repeated low-dose scans were also recorded from some grid regions to assess beam-induced mass loss. The IMPSYS (24) and MASDET (25) program packages were used for evaluation. In short, fibril segments were selected in square boxes and tracked. The total scattering within an integration box following their length was then calculated, and the scattering contribution of the supporting carbon film was subtracted. Division by the segment length gave the MPL. MPL values were corrected for beam-induced mass loss, scaled to the MPL of tobacco mosaic virus, binned, displayed in a histogram, and described by Gaussian curves.

The number of TTR(105-115) peptides per 4.67 Å cross-section was calculated as (MPL x 4.67) / MW where MPL is the fitted mass-per-length (kDa/Å) and MW is the molecular weight of the TTR(105-115) peptide (1.2 kDa).

Calculation of simulated X-ray diffraction pattern:

The simulated X-ray diffraction pattern was generated from the fitted atomic coordinates using the "Fibre Diffraction Simulation" module of the Clearer program (26). Fibre disorder was set to 0.5 rad to closely match the degree of arc of the 4.67 Å meridional reflection. Default values were used for all other parameters. Comparison between the simulated and experimental diffraction patterns revealed that the positions of the 16 reflections are practically identical. It is important to note that the 4.67 ± 0.1 Å meridional reflection is the *average* separation of β-strands within a single sheet and that the 8.86 ± 0.3 Å equatorial reflection is the *average* separation of adjacent β-sheets within individual protofilaments. In the NMR-derived protofilament and NMR/cryo EM-derived fibril structures, the average Cα-Cα separation of two adjacent β-strands within the same sheet is 4.67 ± 0.08 Å and the average Cα-Cα separation of two adjacent β-sheets within individual protofilaments is 8.71 ± 1.92 Å. Thus, all structures are fully consistent with the X-ray fibre diffraction data.

Atomic force microscopy (AFM) imaging:

Solutions of fibrils were diluted by a factor of 10-500 in water at pH 2.0, and 20 μl aliquots were then deposited on to a cleaved mica surface. The surface was left to dry in air for 60 min while being shielded from dust particles. Topographic data were then acquired using a Pico Plus atomic force microscope (Molecular Imaging, Tempe, Arizona, U.S.A.) in tapping mode with Micromasch NCS36 ultrasharp silicon cantilevers. Over 500 height measurements on individual protofilaments resulted in a normal distribution with a statistical average of 38.7±4.4 Å.

Calculation of simulated AFM height profile of filament:

An AFM simulation program (27) was used to calculate the height profile of single filament of the doublet fibril. A tip radius of 100 Å was used in the convolution of the simulated AFM tip with the (.pdb) filament structure.

Molecular dynamics simulations of water bilayer:

Molecular dynamics (MD) simulations were performed with the GROMACS (28) package by using the all-atom Amber99SB force field (29) in combination with the TIP4P-ew explicit water model (30). The simulations were carried out in the NPT ensemble with periodic boundary

conditions at a constant temperature of 300 K. A rectangular box was used to accommodate sections of the TTR(105-115) fibril and a large number of water molecules. We analyzed the MD samplings to compute solvent density maps whose maxima represent the MD hydration sites (31).

Supporting References

1. M. A. Caporini, V. S. Bajaj, M. Veshtort, A. Fitzpatrick, C. E. MacPhee, M. Vendruscolo, C. M. Dobson, R. G. Griffin (2010) Accurate determination of interstrand distances and alignment in amyloid fibrils by magic angle spinning NMR. *J. Phys. Chem. B* 114:13555-13561.
2. T. Karlsson, J. M. Popham, J. R. Long, N. Oyler, G. P. Drobny (2003) A study of homonuclear dipolar recoupling pulse sequences in solid-state nuclear magnetic resonance. *J. Am. Chem. Soc.* 125:7394-7407.
3. T. Gullion, J. Schaefer (1989) Rotational-echo double-resonance NMR. *J. Mag. Res.* 81:196-200.
4. A. E. Bennett, C. M. Rienstra, M. Auger, K. V. Lakshmi, R. G. Griffin (1995) Heteronuclear decoupling in rotating solids. *J. Chem. Phys.* 103:6951-6958.
5. V. Ladizhansky, R. G. Griffin (2004) Band-selective carbonyl to aliphatic side chain C-13-C-13 distance measurements in u-C-13,N-15-labeled solid peptides by magic angle spinning NMR. *J. Am. Chem. Soc.* 126:948-958.
6. N. M. Szeverenyi, M. J. Sullivan, G. E. Maciel (1982) Observation of spin exchange by two-dimensional fourier-transform C-13 cross polarization-magic-angle spinning. *J. Mag. Res.* 47:462-475.
7. C. P. Jaroniec, C. Filip, R. G. Griffin (2002) 3D tedor NMR experiments for the simultaneous measurement of multiple carbon-nitrogen distances in uniformly C-13, N-15-labeled solids. *J. Am. Chem. Soc.* 124:10728-10742.
8. F. Delaglio, S. Grzesiek, G. W. Vuister, G. Zhu, J. Pfeifer, A. Bax (1995) Nmrpipe - a multidimensional spectral processing system based on unix pipes. *J. Biomol. NMR* 6:277-293.
9. T. D. Goddard, D. G. Kneller (Sparky 3.115. University of california, san francisco.
10. C. R. Morcombe, K. W. Zilm (2003) Chemical shift referencing in mas solid state NMR. *J. Mag. Res.* 162:479-486.
11. M. Veshtort, R. G. Griffin (2006) Spinevolution: A powerful tool for the simulation of solid and liquid state NMR experiments. *J. Mag. Res.* 178:248-282.
12. A. T. Brunger (2007) Version 1.2 of the crystallography and NMR system. *Nat. Prot.* 2:2728-2733.
13. C. P. Jaroniec, C. E. MacPhee, V. S. Bajaj, M. T. McMahon, C. M. Dobson, R. G. Griffin (2004) High-resolution molecular structure of a peptide in an amyloid fibril determined by magic angle spinning NMR spectroscopy. *Proc. Natl. Acad. Sci. USA* 101:711-716.
14. S. I. O'Donoghue, M. Nilges (2002) Calculation of symmetric oligomer structures from NMR data. *Biol. Mag. Res.* 17:131-161.

15. R. A. Laskowski, J. A. C. Rullmann, M. W. MacArthur, R. Kaptein, J. M. Thornton (1996) Aqua and procheck-NMR: Programs for checking the quality of protein structures solved by NMR. *J. Biomol. NMR* 8:477-486.

16. J. L. Jimenez, J. L. Guijarro, E. Orlova, J. Zurdo, C. M. Dobson, M. Sunde, H. R. Saibil (1999) Cryo-electron microscopy structure of an SH3 amyloid fibril and model of the molecular packing. *EMBO J.* 18:815-821.

17. C. Sachse, J. Z. Chen, P. D. Coureux, M. E. Stroupe, M. Fandrich, N. Grigorieff (2007) High-resolution electron microscopy of helical specimens: A fresh look at tobacco mosaic virus. *J. Mol. Biol.* 371:812-835.

18. J. A. Mindell, N. Grigorieff (2003) Accurate determination of local defocus and specimen tilt in electron microscopy. *J. Struct. Biol.* 142:334-347.

19. J. Frank, M. Radermacher, P. Penczek, J. Zhu, Y. H. Li, M. Ladjadj, A. Leith (1996) Spider and web: Processing and visualization of images in 3D electron microscopy and related fields. *J. Struct. Biol.* 116:190-199.

20. M. vanHeel, G. Harauz, E. V. Orlova, R. Schmidt, M. Schatz (1996) A new generation of the imagic image processing system. *J. Struct. Biol.* 116:17-24.

21. C. Sachse, M. Fandrich, N. Grigorieff (2008) Paired beta-sheet structure of an a beta(1-40) amyloid fibril revealed by electron microscopy. *Proc. Natl. Acad. Sci. USA* 105:7462-7466.

22. I. M. Orlov, D. G. Morgan, R. H. Cheng (2006) Efficient implementation of a filtered back-projection algorithm using a voxel-by-voxel approach. *J. Struct. Biol.* 154:287-296.

23. E. F. Pettersen, T. D. Goddard, C. C. Huang, G. S. Couch, D. M. Greenblatt, E. C. Meng, T. E. Ferrin (2004) UCSF chimera - a visualization system for exploratory research and analysis. *J. Comp. Chem.* 25:1605-1612.

24. S. A. Muller, A. Engel (1998) Mass measurement in the scanning transmission electron microscope: A powerful tool for studying membrane proteins. *J. Struct. Biol.* 121:219-230.

25. V. Krzyzanek, S. A. Muller, A. Engel, R. Reichelt (2009) Masdet-a fast and user-friendly multiplatform software for mass determination by dark-field electron microscopy. *J. Struct. Biol.* 165:78-87.

26. O. S. Makin, P. Sikorski, L. C. Serpell (2007) Clearer: A new tool for the analysis of X-ray fibre diffraction patterns and diffraction simulation from atomic structural models. *J. Appl. Cryst.* 40:966-972.

27. G. Varadhan, W. Robinett, D. Erie, R. M. Taylor (2002) Fast simulation of atomic-force-microscope imaging of atomic and polygonal surfaces using graphics hardware. *Visualization and data analysis 2002,* Proceedings of the society of photo-optical instrumentation engineers (spie), eds Erbacher RF, Chen PC, Grohn M, Roberts JC, & Wittenbrink CM), Vol 4665, pp 116-124.

28. B. Hess, C. Kutzner, D. van der Spoel, E. Lindahl (2008) Gromacs 4: Algorithms for highly efficient, load-balanced, and scalable molecular simulation. *J. Chem. Theor. Comp.* 4:435-447.

29. V. Hornak, R. Abel, A. Okur, B. Strockbine, A. Roitberg, C. Simmerling (2006) Comparison of multiple amber force fields and development of improved protein backbone parameters. *Proteins* 65:712-725.

30. H. W. Horn, W. C. Swope, J. W. Pitera, J. D. Madura, T. J. Dick, G. L. Hura, T. Head-Gordon (2004) Development of an improved four-site water model for biomolecular simulations: Tip4p-ew. *J. Chem. Phys.* 120:9665-9678.

31. L. Vitagliano, R. Berisio, A. De Simone (2011) Role of hydration in collagen recognition by bacterial adhesins. *Bioph. J.* 100:2253-2261.
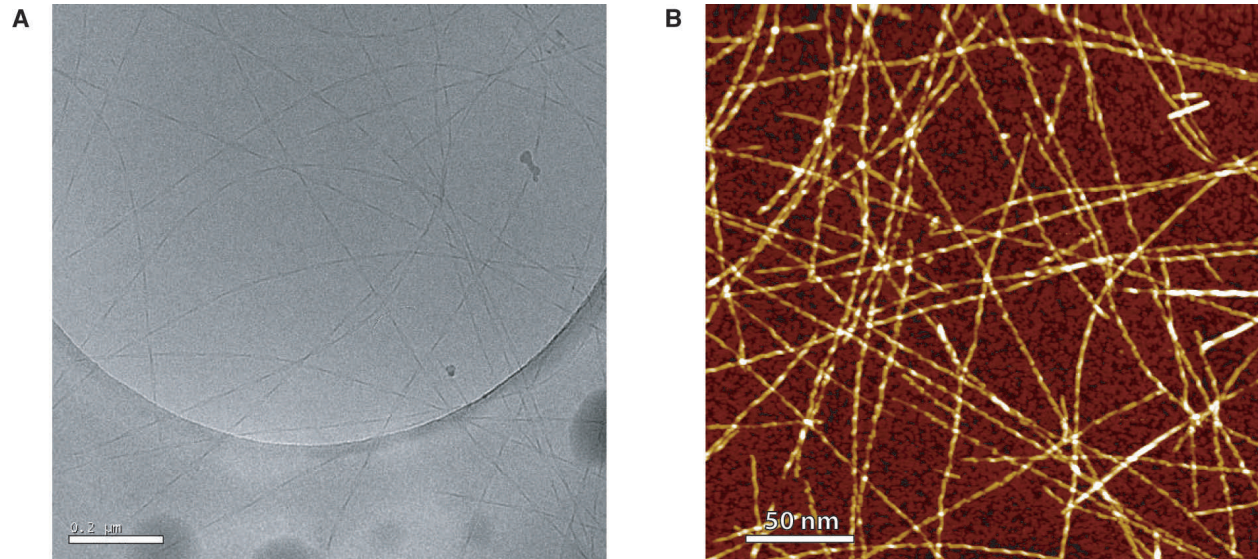
Supporting Figures

Figure S1. Images of mature TTR(105-115) fibrils taken using (A) cryo-EM at 15000x magnification (scale bar 200 nm) and (B) AFM imaging on a 2mg/ml sample (scale bar 50 nm).
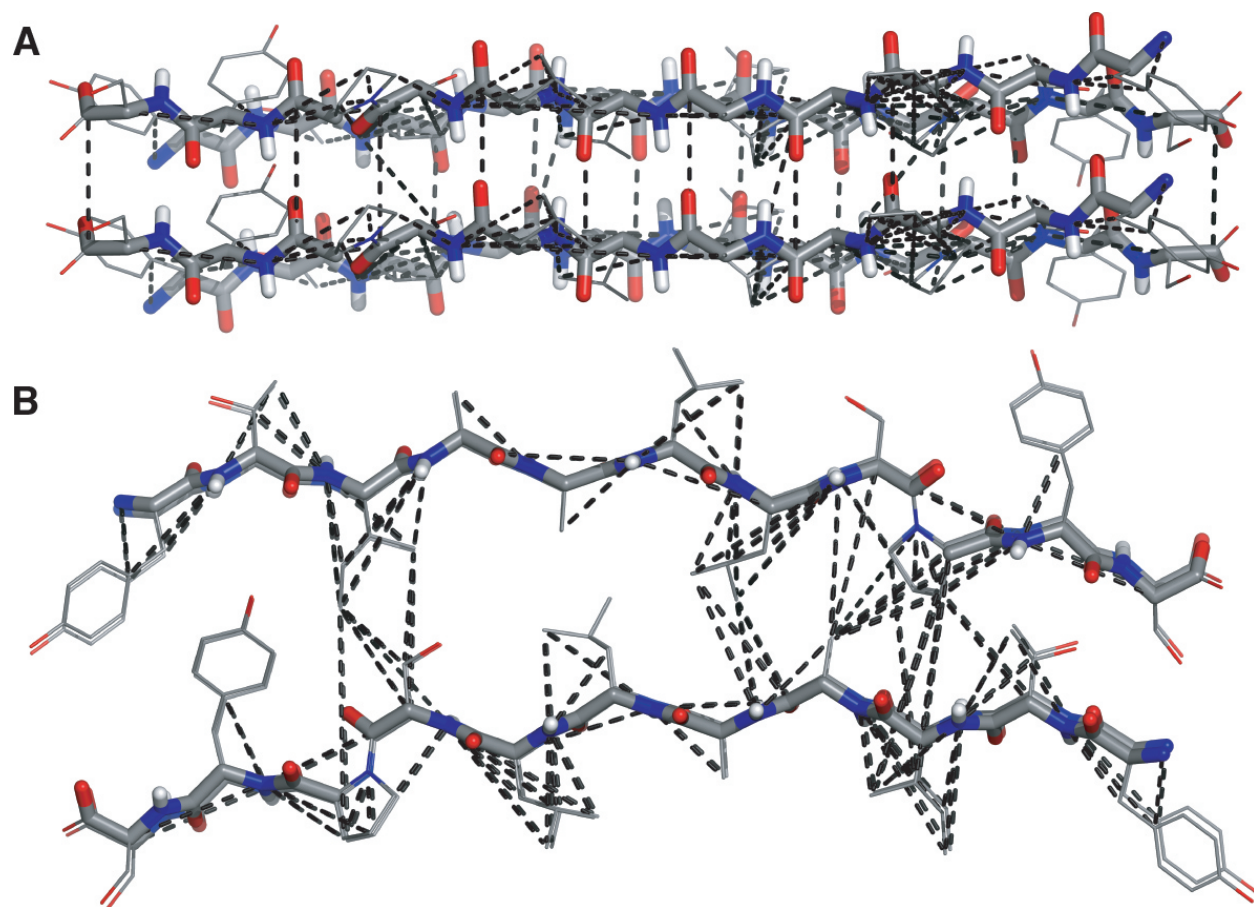
Figure S2. Structure of the TTR(105-115) protofilament with intramolecular (27), intra-sheet (Table S1) and inter-sheet (Table S2) NMR distance restraints (black dashed lines) superimposed. (A) Short section of the protofilament viewed at right angles to the long axis of the fibril. (B) View of the protofilament looking down the long axis of the fibril.
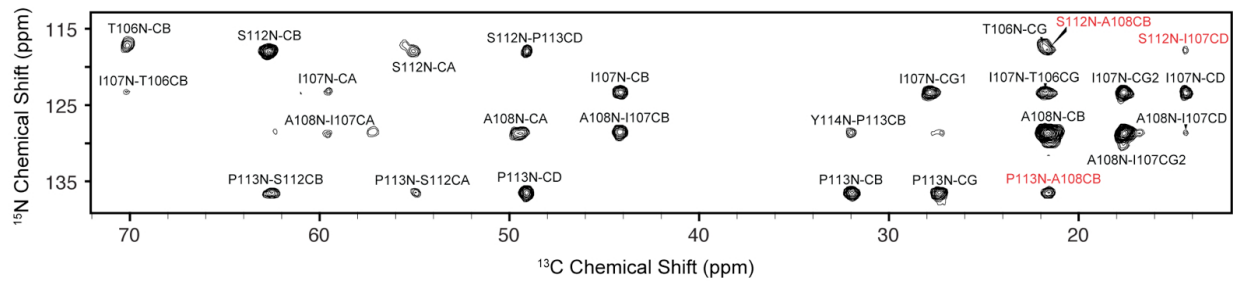
Figure S3. ^{15}N-^{13}C spectrum obtained with TEDOR mixing (τ_{mix} = 10.24 ms) with a U-^{13}C,^{15}N **YTIA**ALL**SPY**S labeled TTR(105-115) fibril sample. Inter-sheet correlations are labeled in red.

Figure S4. ^{13}C-^{13}C correlation spectrum obtained at 900 MHz, $\omega_r/2\pi$=11.0 kHz and 200 ms PDSD mixing with a U-^{13}C,^{15}N **YTIA**ALL**SPY**S labeled TTR(105-115) fibril sample. The observed inter-sheet correlations are labeled in red.
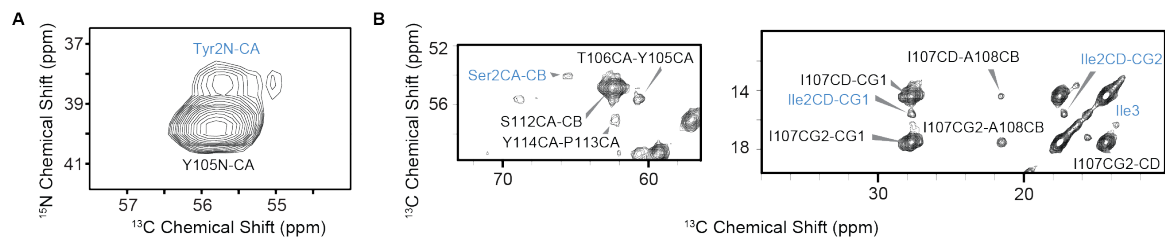
Figure S5. Spectra illustrating that for some residues multiple peaks are observed. (A) One-bond NCA correlation spectrum of a TTR(105-115) sample, uniformly ^{13}C,^{15}N labeled at **YTIA**ALL**SPY**S. Only the region corresponding to the N-terminal Y105N-Cα crosspeaks is shown. Two different conformations of the N-terminal residue are observed, with ^{15}N chemical shifts of 39.8 and 38.3 ppm. The spectrum was recorded with TEDOR mixing (τ_{mix} = 1.8 ms) on a spectrometer operating at 750 MHz ^{1}H Larmor frequency. (B) Sections from a PDSD spectrum obtained at 900 MHz ^{1}H Larmor frequency with τ_{mix} = 100 ms with the same sample. S112 and I107 display peak multiplicity. Peak multiplicities were reproducibly observed in independent sample preparations.
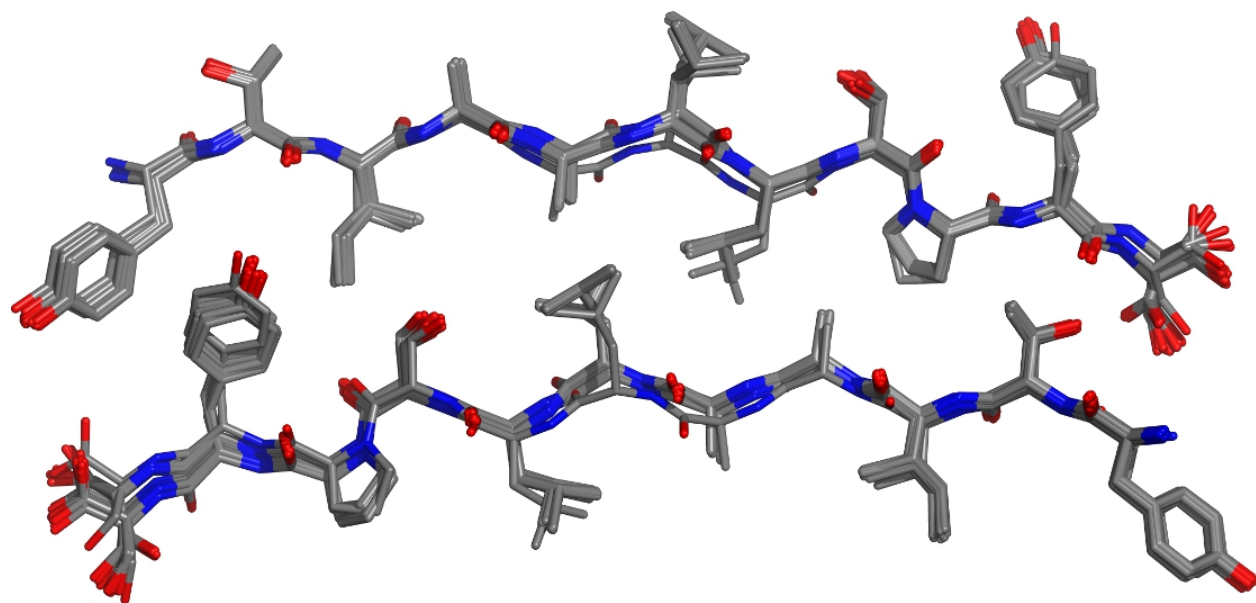
Figure S6. Ensemble of the 20 lowest-energy protofilament structures. For clarity, only a single layer of the protofilament is shown.
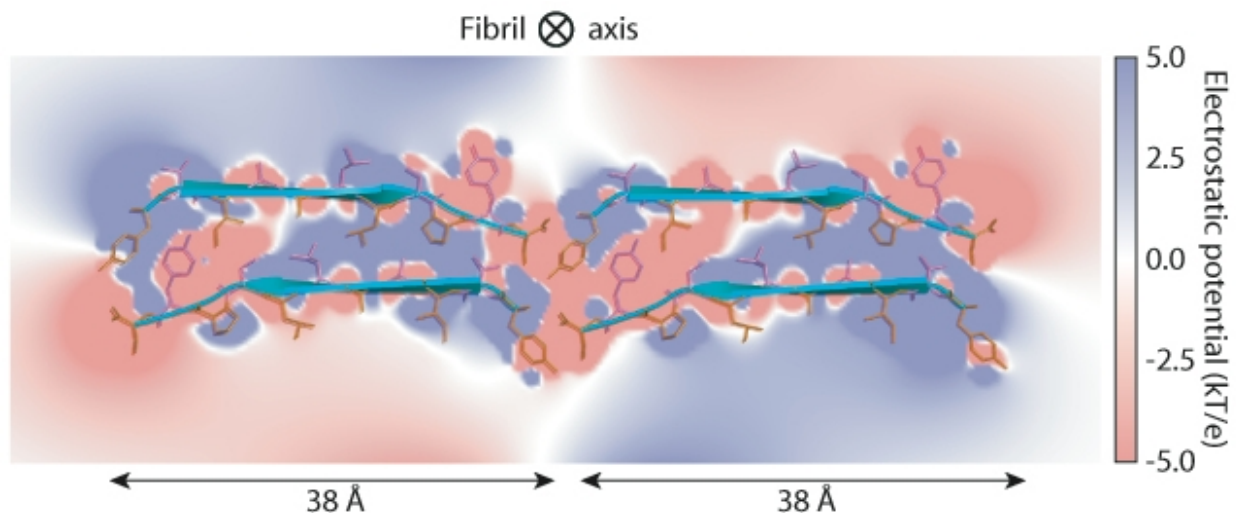
Figure S7. Protofilament-protofilament interface viewed looking down the long axis of the fibril showing the head-to-tail packing arrangement. A cross-section of the electrostatic potential surface of the protofilament-protofilament complex is shown ranging from +5 kT/e (blue) to -5 kT/e (red) with white representing uncharged regions of the constituent peptides. For clarity, an overlaid ribbon and stick representation makes individual sidechains more identifiable.
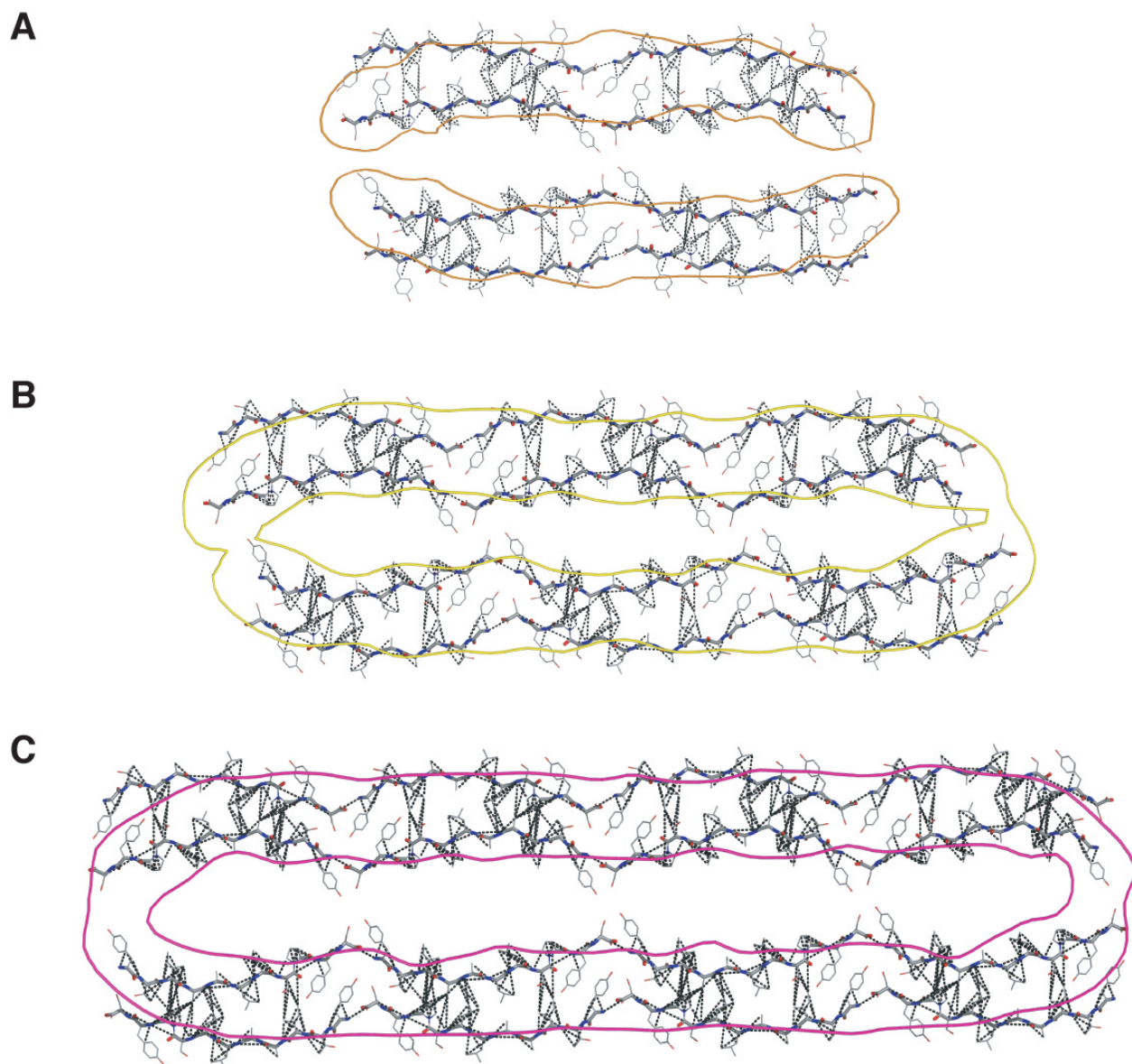
Figure S8. Cross sections of the (A) doublet, (B) triplet and (C) quadruplet fibril structures with intramolecular (27), intra-sheet (Table S1), inter-sheet (Table S2), interprotofilament (distance between S115-$^{13}CO_2^-$--$^{15}NH_3^+$-Y105 is 3.57±0.06 Å) NMR distance restraints (black dashed lines) and cryo-EM envelopes (orange, yellow and purple contours at 1.0σ above the mean density for doublet, triplet and quadruplet fibrils respectively) superimposed.
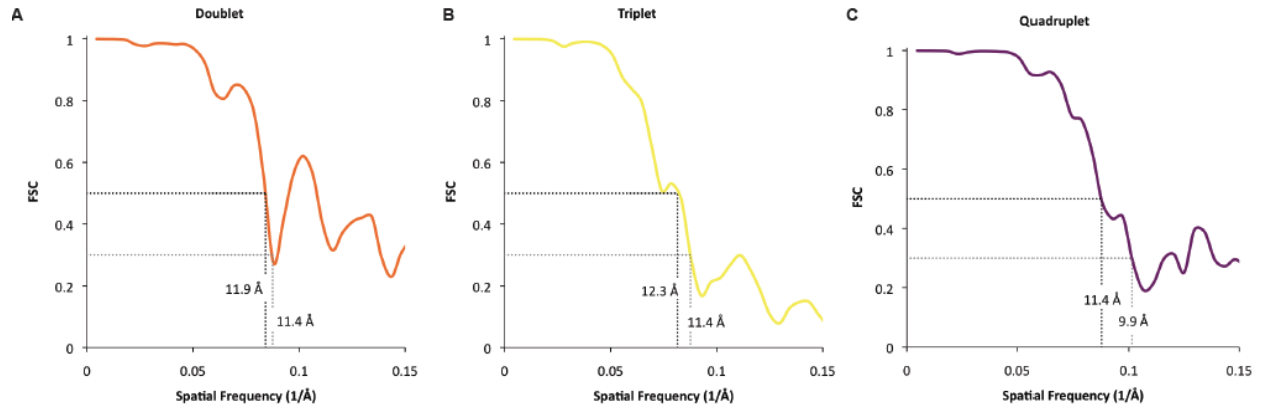
Figure S9. Fourier shell correlation (FSC) of the TTR(105-115) fibril three-dimensional reconstructions. The black dotted lines correspond to the FSC = 0.5 positions and the gray dotted lines show FSC = 0.3 positions. Doublet, 11.9 Å (FSC, 0.5), 11.4 Å (FSC, 0.3); Triplet, 12.3 Å (FSC, 0.5), 11.4 Å (FSC, 0.3); Quadruplet, 11.4 Å (FSC, 0.5), 9.9 Å (FSC, 0.3).
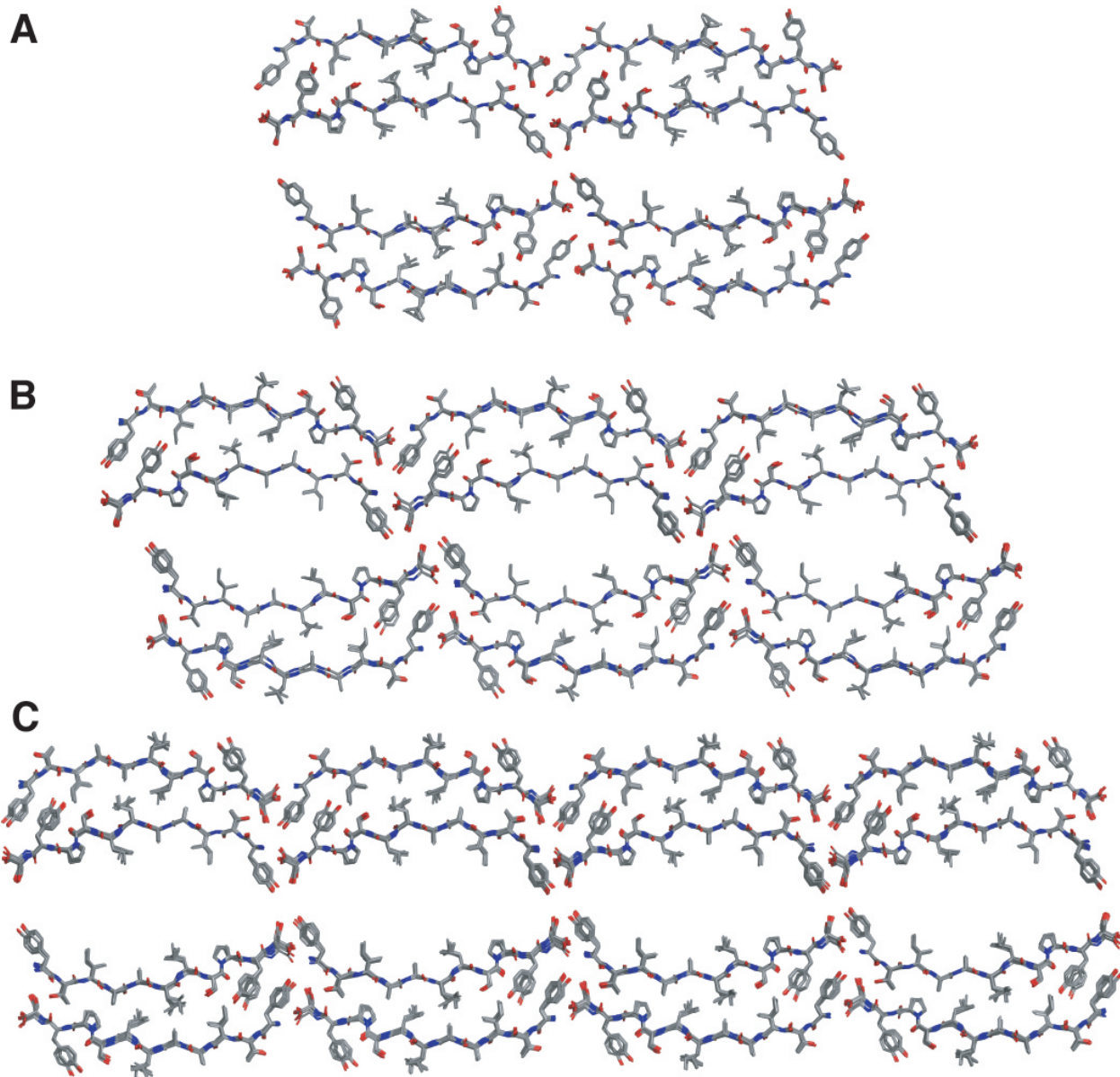
Figure S10. Ensemble of the 20 lowest-energy (A) doublet, (B) triplet and (C) quadruplet fibril structures. For clarity, only a single layer of each of the fibril polymorphs is shown.
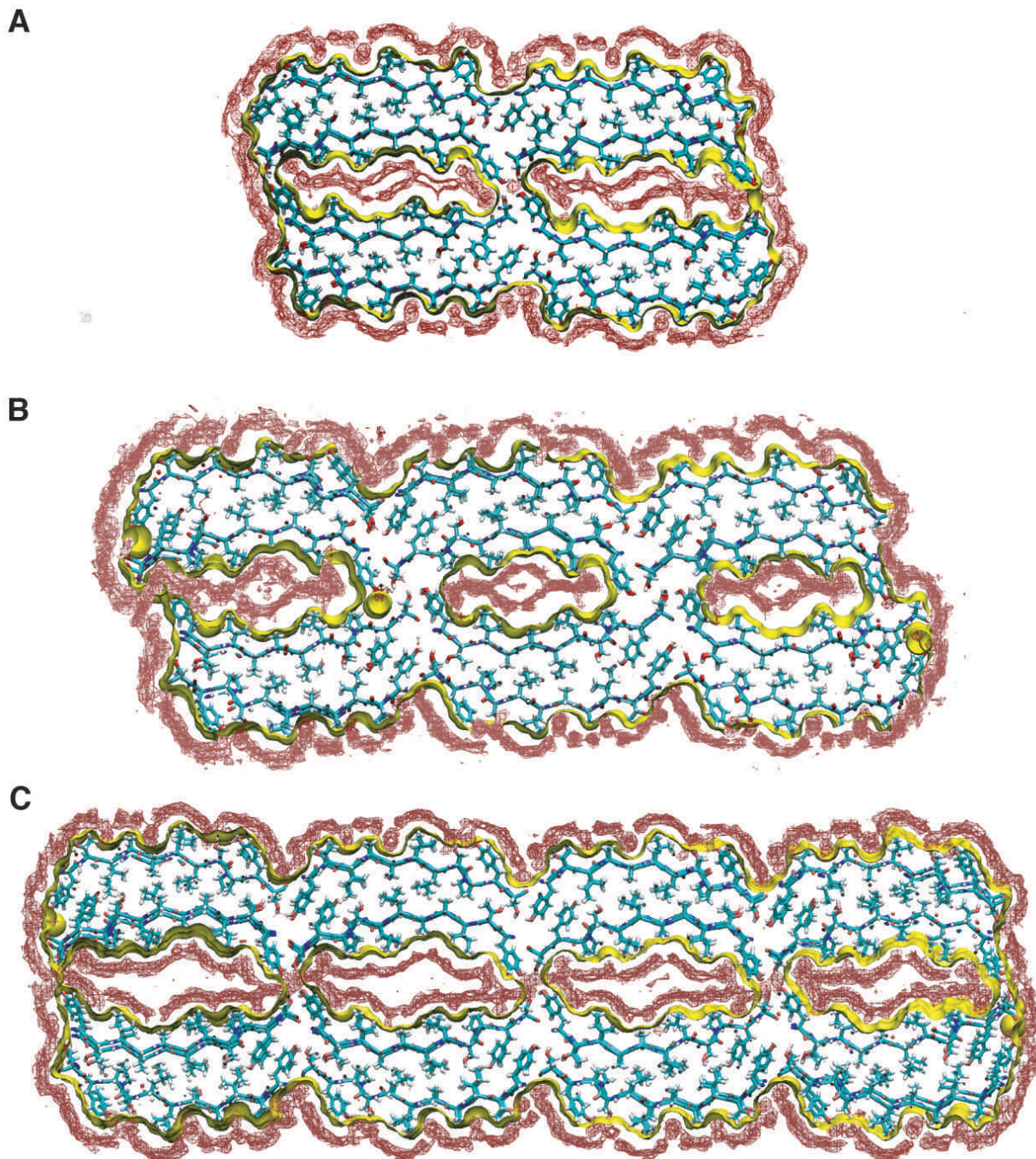
Figure S11. Water solvation maps of the (A) doublet, (B) triplet and (C) quadruplet fibril with oxygen, carbon, nitrogen and hydrogen atoms shown as red, cyan, blue and white sticks respectively with a cross section through the molecular surface coloured yellow. The maps show that on average there is a water bilayer (water density shown in red) in the elongated cavity separating the protofilaments. The simulated maps also demonstrate that no H_2O molecules penetrate into the dry two-sheet protofilaments.
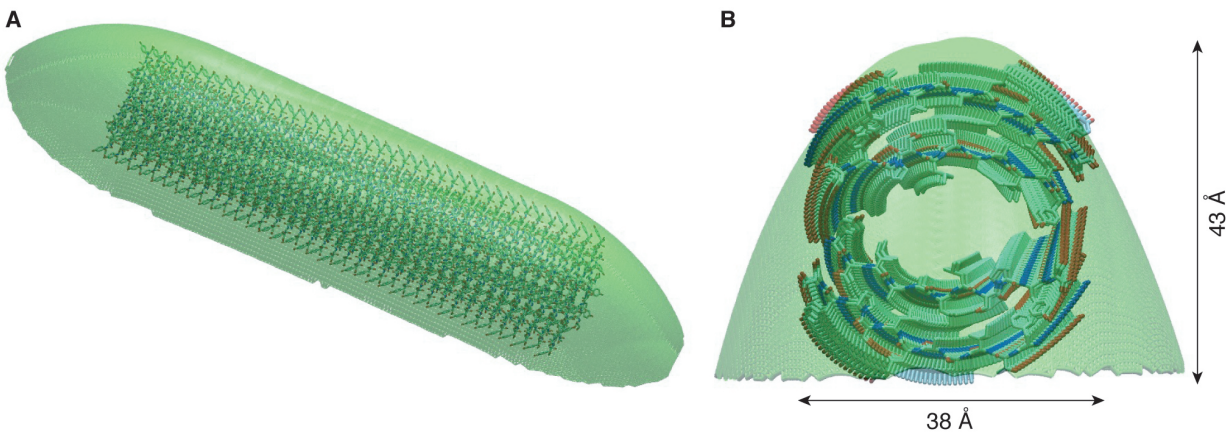
Figure S12. Simulated AFM surface from the convolution of an artificial 100 Å AFM tip with the coordinates of the TTR(105-115) filament structure. (A) View from above looking down on to the surface traced out by a simulated AFM tip. (B) Cross-sectional view of the simulated AFM profile of the filament showing its near-uniform height dimensions (38 Å x 43 Å). The simulated height profile of a filament matches perfectly with the constant experimental height of 38.7 ± 4.4 Å.

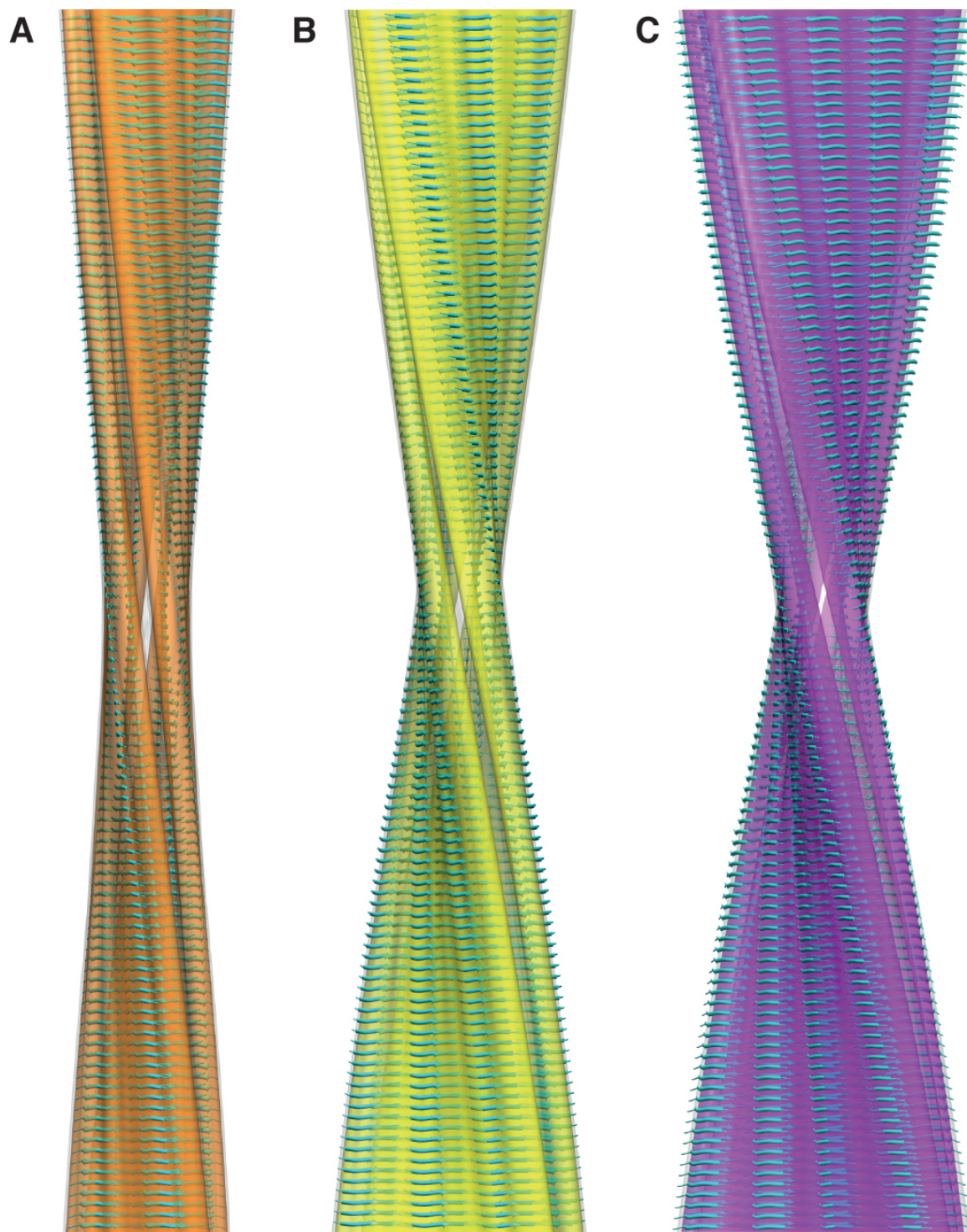**Figure S13.** Atomic resolution structures of amyloid fibrils formed by TTR(105-115). MAS NMR atomic structures fitted into cryo-EM reconstructions of the (A) double, (B) triplet and (C) quadruplet fibrils. The outer fibril surfaces are shown as semi-transparent solid surfaces (white and coloured surfaces at 1.0σ and 2.2σ above the mean density respectively) and the constituent β-sheets are shown in a ribbon representation.

Figure S14. Close-up view of the MAS NMR atomic-resolution structure of the doublet fibril fitted into the cryo-EM reconstruction. The background image of the fibril in the left panel was taken with a transmission electron microscope (scale bar, 12.5 nm). The fibril surfaces in the right panel are shown at 1.0σ (white) and 2.2σ (yellow) above the mean density, respectively, and the constituent β-sheets are shown in a ribbon representation; oxygen, carbon, and nitrogen atoms are shown as red, gray, and blue sticks, respectively.
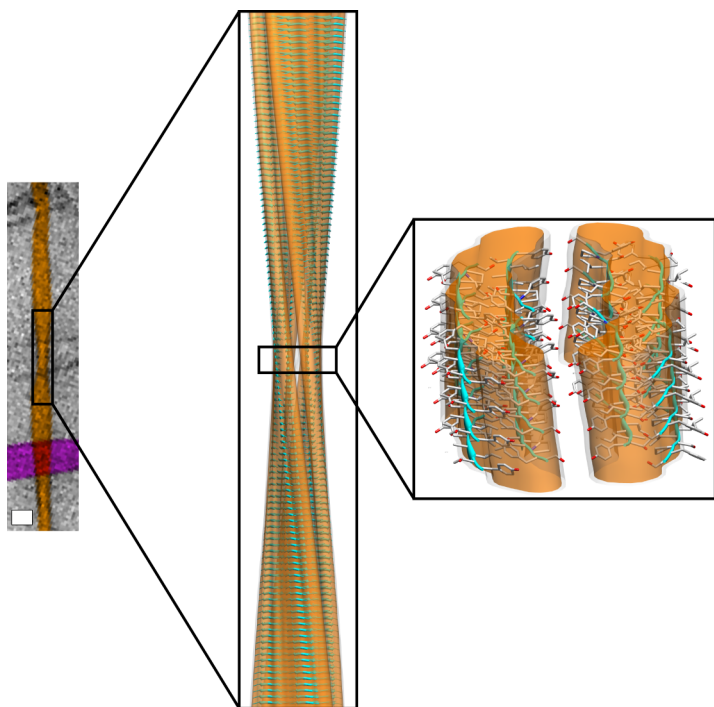
Figure S15. Close-up view of the MAS NMR atomic-resolution structure of the quadruplet fibril fitted into the cryo-EM reconstruction. The background image of the fibril in the left panel was taken with a transmission electron microscope (scale bar, 25 nm). The fibril surfaces in the right panel are shown at 1.0σ (white) and 2.2σ (yellow) above the mean density, respectively, and the constituent β-sheets are shown in a ribbon representation; oxygen, carbon, and nitrogen atoms are shown as red, gray, and blue sticks, respectively.
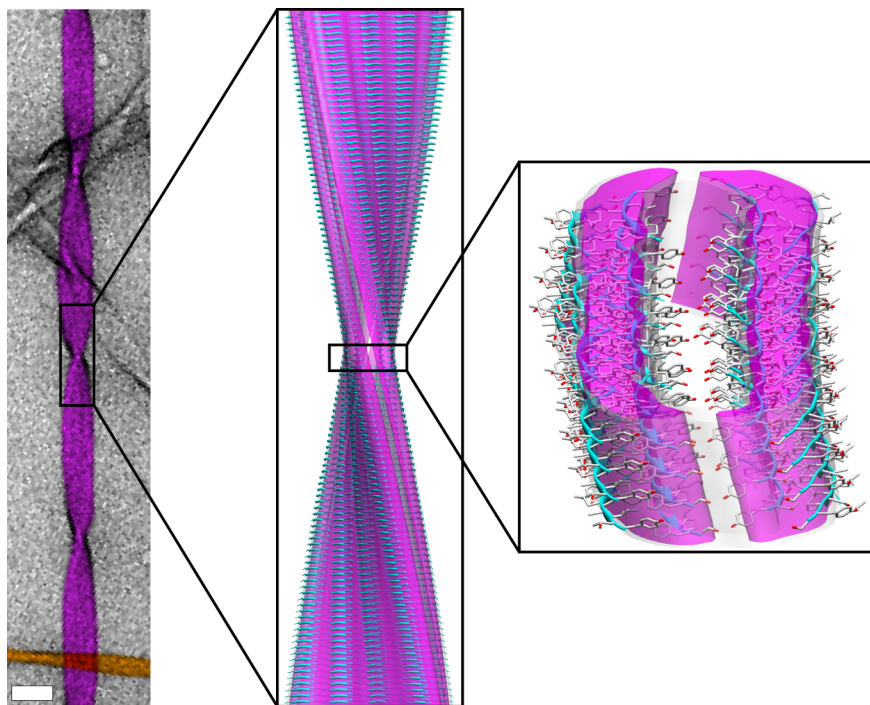
Supporting Tables

Table S1. Intra-sheet NMR restraints.

Residue-Atom	Residue-Atom	Distance (Å)	Method
I107-CO	I107-CO	4.51 +/- 0.13	DQF-DRAWS
A108-CO	A108-CO	4.59 +/- 0.15	DQF-DRAWS
A109-CO	A109-CO	4.47 +/- 0.09	DQF-DRAWS
L110-CO	L110-CO	4.41 +/- 0.22	DQF-DRAWS
L111-CO	L111-CO	4.52 +/- 0.10	DQF-DRAWS
S112-CO	S112-CO	4.48 +/- 0.05	DQF-DRAWS
P113-CO	P113-CO	4.52 +/- 0.08	DQF-DRAWS
S115-CO	S115-CO	4.29 +/- 0.05	DQF-DRAWS
A109-N	A108-CO	4.40 +/- 0.20	REDOR

Table S2. Inter-sheet NMR restraints.

Residue-Atom	Residue-Atom	Distance (Å)	Method
I107-Cδ1	S112-N	5.8 +/- 0.5	TEDOR
A108-Cβ	S112-N	5.4 +/- 0.5	TEDOR
A108-Cβ	P113-N	6.0 +/- 0.4	TEDOR
A109-N	L111-Cδ1	4.4 +/- 0.5	TEDOR
A109-N	L111-Cδ2	4.6 +/- 0.5	TEDOR
A108-CO	L111-Cδ1	4.8 +/- 0.5	R2TR
A108-CO	L111- Cδ2	4.8 +/- 0.5	R2TR
T106-Cα	P113-Cβ	2.5-6.5	PDSD
II07-Cα	P113-Cα	2.5-6.5	PDSD
I107-Cα	P113-Cβ	2.5-6.5	PDSD
I107-Cβ	P113-Cβ	2.5-4.5	PDSD
I107-Cβ	P113- Cδ	2.5-8.5	PDSD
I107- Cδ1	S112-Cα	2.5-4.5	PDSD
I107- Cδ1	S112-Cβ	2.5-4.5	PDSD
I107- Cδ1	P113-Cβ	2.5-8.5	PDSD
I107-Cγ2	S112-Cα	2.5-6.5	PDSD
I107-Cγ2	S112-Cβ	2.5-6.5	PDSD
I107-Cγ2	P113-Cα	2.5-8.5	PDSD
I107-Cγ2	P113-Cβ	2.5-8.5	PDSD
A108-Cβ	S112-Cα	2.5-6.5	PDSD
A108-Cβ	P113-Cα	2.5-4.5	PDSD
A108-Cβ	P113-Cβ	2.5-4.5	PDSD
A108-Cβ	P113-Cγ	2.5-4.5	PDSD

Table S3. Experimental restraints and structural statistics for ensembles of the twenty lowest-energy protofilament, doublet, triplet and quadruplet structures.

	Protofilament	Doublet	Triplet	Quadruplet
Number of experimental restraints (per peptide):				
Unambiguous	67	68*	69*	69*
Dihedral restraints	41	41	41	41
Total experimental restraints	108	109	110	110
Distance restraint violations > 0.3 Å	0	0	0	0
Dihedral angle violations > 5°	0	0	0	0
RMS deviations:				
From the experimental restraints:				
Distance restraints (Å)	3.7×10^{-2} $\pm 9.7 \times 10^{-4}$	3.6×10^{-2} $\pm 7.1 \times 10^{-4}$	3.6×10^{-2} $\pm 3.0 \times 10^{-4}$	3.7×10^{-2} $\pm 6.0 \times 10^{-4}$
Dihedral angles (°)	0.54 ± 0.07	0.56 ± 0.12	0.81 ± 0.14	0.73 ± 0.15
From idealised geometry:				
Bonds (Å)	1.4×10^{-3} $\pm 7.5 \times 10^{-5}$	1.5×10^{-3} $\pm 9.2 \times 10^{-5}$	1.6×10^{-3} $\pm 1.2 \times 10^{-5}$	1.6×10^{-3} $\pm 1.0 \times 10^{-4}$
Angles (°)	0.31 ± 0.01	0.33 ± 0.01	0.32 ± 0.01	0.33 ± 0.01
Improper angles (°)	0.16 ± 0.02	0.21 ± 0.01	0.23 ± 0.003	0.23 ± 0.01
Coordinate RMSD**:				
Backbone (Å)	0.43	0.44	0.60	0.59
All heavy atom (Å)	0.68	0.59	0.72	0.73
Ramachandran Analysis:				
Residues in most favoured regions	87.5%	87.5%	87.5%	87.5%
Residues in additionally allowed regions	12.5%	12.5%	12.5%	12.5%
Residues in generously allowed regions	0%	0%	0%	0%
Residues in disallowed regions	0%	0%	0%	0%

* There is one (two) additional restraint per peptide for the doublet (triplet and quadruplet) structure calculation owing to the inclusion of the inter-protofilament distance restraint (the distance between S115-$^{13}CO_2^-$--$^{15}NH_3^+$-Y105 in adjacent protofilaments is 3.57±0.06 Å).

** The rms deviation of the backbone and heavy atoms for the full-length (Y105-S115) peptide in the ensemble of twenty lowest-energy structures. All structures (protofilament, doublet, triplet and quadruplet) are composed of β-sheets containing 8 β-strands.

Table S4. Cryo-EM image processing statistics.

	Doublet	Triplet	Quadruplet
Number of class averages used for reconstruction	18	28	31
Images per class	4	5	5
Number of fibrils	82	152	175
Pixel size, Å	1.8	1.8	1.8
Segment size, Å	216 x 216	216 x 216	216 x 216
Segment step size, Å	36	36	36
Number of segments	702	1092	1209
Width in peptide chain direction, Å	84	121	154
Wet interface, Å (at 1σ threshold)	12.2±1.2	10.7±0.8	14.1±0.9
Subunit repeat, Å	4.67	4.67	4.67
Average crossover, Å	995	911	948
Inter-strand twist, °	0.85	0.93	0.89
Map resolution at FSC 0.5/0.3, Å	12.7/11.8	12.2/11.3	11.6/9.7

Supporting Equation

Handedness of the fibrils:

The twist of the fibrils is a result of the left-handed chirality of the amino acids, which causes a right-handed twist along the peptide backbone, inducing a left-handed twist in the direction orthogonal to the peptide chain (the long axis of the fibril).

The twist angle, θ, between successive β-strands in the direction of the long axis of the NMR-derived protofilament structure was calculated as

$$\theta = \frac{1}{(n-m)} \cos^{-1}(\hat{u}_m . \hat{u}_n)$$

where $\hat{u}_m$ is the unit vector from the Cα atom of residue 1 to the Cα atom of residue 11 and m and n are the first and last chains considered respectively. Using the (x,y,z) coordinates of the Cα atoms at the termini of the peptides, the inter-strand twist within the fibril sample was calculated to be ~1° in the left-handed direction.

Supporting Information

Fitzpatrick et al. 10.1073/pnas.1219476110

SI Text

Present Addresses for Authors. Anthony W. P. Fitzpatrick: Physical Biology Center for Ultrafast Science and Technology, Arthur Amos Noyes Laboratory of Chemical Physics, California Institute of Technology, Pasadena, CA 91125.

Galia T. Debelouchina: Department of Chemistry, Princeton University, Princeton, NJ 08544.

Marvin J. Bayro: Laboratory of Chemical Physics, National Institutes of Health, Bethesda, MD 20892.

Marc A. Caporini: Bruker-BioSpin, Manning Park, Billerica, MA 01821.

Vikram S. Bajaj: Department of Chemistry, University of California, Berkeley, CA 94720-3220.

Christopher P. Jaroniec: Department of Chemistry, Ohio State University, Columbus, OH 43210.

Vladimir Ladizhansky: Department of Physics, University of Guelph, Guelph, ON, Canada N1G 2W1.

Shirley A. Müller: Center for Cellular Imaging and Nano Analytics, Biozentrum, CH-4058 Basel, Switzerland.
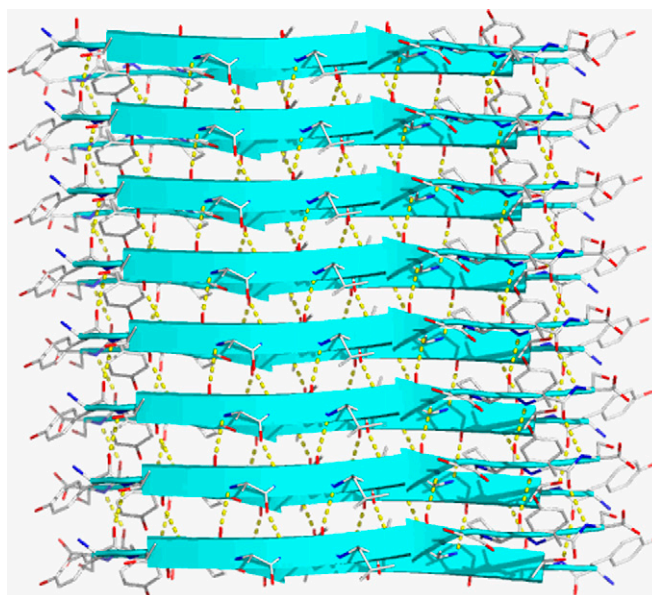
Movie S1. Shown is a rotating view of the two-sheet atomic-resolution protofilament structure formed by TTR(105–115). The protofilament is viewed at right angles to the long axis of the fibril with oxygen, carbon, and nitrogen shown as red, white, and blue sticks, respectively. Secondary structure is shown in a cyan ribbon representation and hydrogen bonds as yellow dashes. By following the rotating structure, the parallel, hydrogen-bonded intrasheet packing of β-strands and the antiparallel, staggered stacking of the two β-sheets are clearly evident.
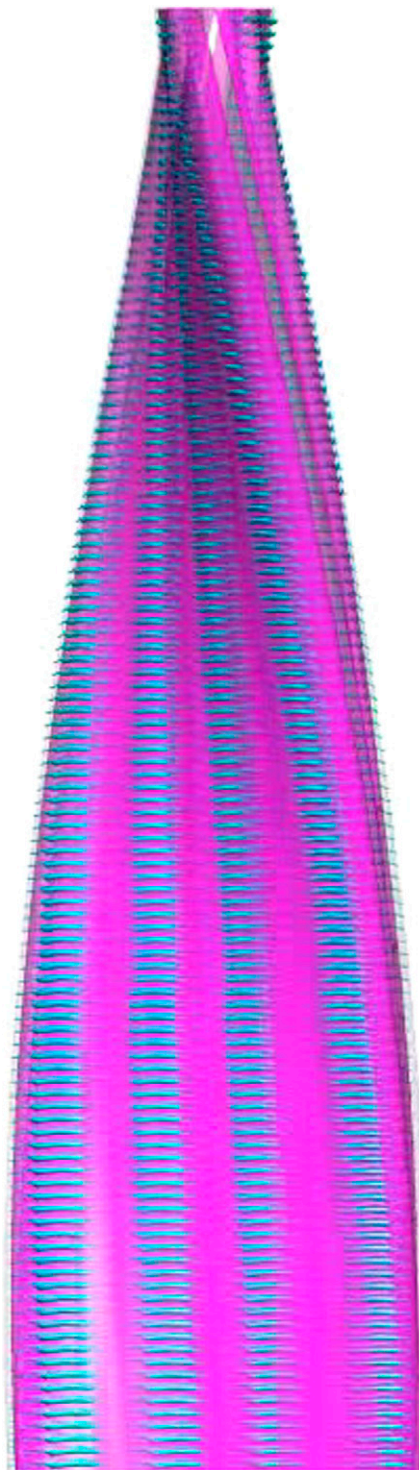
Movie S1

Movie S2. Shown is a rotating view of the atomic-resolution doublet fibril structure formed by TTR(105–115). The fibril is viewed at right angles to the long axis of the fibril, with the outer fibril surface shown as semitransparent solid surfaces (white and orange electron density surfaces at 1.0σ and 2.2σ above the mean density, respectively), and the constituent β-sheets are shown in a ribbon representation. By following the rotating structure, the twisted fibril ultrastructure and the four-protofilament substructure can be seen. The cavity corresponding to the wet interface between paired β-sheets is clearly visible as a hollow seam running up the outside of the left-handed helical fibrils.

[Movie S2](#)

Movie S3.   Shown is a rotating view of the atomic-resolution triplet fibril structure formed by TTR(105–115). The fibril is viewed at right angles to the long axis of the fibril, with the outer fibril surface shown as semitransparent solid surfaces (white and yellow electron density surfaces at 1.0σ and 2.2σ above the mean density, respectively) and the constituent β-sheets are shown in a ribbon representation. By following the rotating structure, the twisted fibril ultrastructure and the six-protofilament substructure can be seen. The cavity corresponding to the wet interface between paired β-sheets is clearly visible as a hollow seam running up the outside of the left-handed helical fibrils.

[Movie S3](#)

Movie S4. Shown is a rotating view of the atomic-resolution quadruplet fibril structure formed by TTR(105–115). The fibril is viewed at right angles to the long axis of the fibril, with the outer fibril surface shown as semitransparent solid surfaces (white and purple electron density surfaces at 1.0σ and 2.2σ above the mean density, respectively), and the constituent β-sheets are shown in a ribbon representation. By following the rotating structure, the twisted fibril ultrastructure and the eight-protofilament substructure can be seen. The cavity corresponding to the wet interface between paired β-sheets is clearly visible as a hollow seam running up the outside of the left-handed helical fibrils.

Movie S4

Other Supporting Information Files